FINAL TECHNICAL REPORT: FY 1995/1996

Name of Contractor: University of Washington

Principal Investigator:

R.S. Crosson
Geophysics Program
Box 351650
University of Washington
Seattle, WA 98195-1650

Government Technical Officer:

Dr. John Unger
MS 905
U.S. Geological Survey
12201 Sunrise Valley Drive
Reston, VA 20192

Short Title: Earthquake Hazard Research In the
                                   Pacific Northwest using WRSN Data

Program objective number: I-1

Effective Date: May 1, 1995

Amount: $54,973

Time Period Covered in Report: May/1/95 - 4/30/97

Date Report Submitted: Oct. 16, 1998

CONTENTS

      Dewberry, S. R., and R. S. Crosson
          Source scaling and moment estimation for the Pacific Northwest Seismograph
          Network using S-coda amplitude, BSSA, V. 85, pp. 1309-1326, 1995.

      Dewberry, S. R., and R. S. Crosson
          The M_D earthquake of 29 January 1995 in the Puget Lowland
          of western Washington: an event on the Seattle fault?, BSSA,
          V. 86, N. 4, pp. 1167-1172, 1996.

      Schultz, A. P., and R. S. Crosson
          Seismic velocity profile across the central Washington Cascade Range from
          refraction interpretation with earthquake sources, JGR (B),
          V. 101, N.12, pp. 27,899-27,915, 1996.

      Thomas, G.C., R. S. Crosson, D. L. Carver and T. S. Yelin
          The 25 March 1993 Scotts Mills, Oregon earthquake and aftershock sequence:
          Spatial distribution, focal mechanisms, and the Mt. Angel Fault, BSSA
          V. 86, N. 4, pp. 925-935, 1996.

EARTHQUAKE HAZARD RESEARCH IN THE PACIFIC NORTHWEST USING WASHINGTON REGIONAL SEISMOGRAPH NETWORK DATA

Robert S. Crosson
University of Washington
GEOPHYSICS Box 351650
Seattle, WA 98195-1650
Phone:(206)543-6505 FAX:(206)543-0489 E-mail:crosson@u.washington.edu

NON-TECHNICAL ABSTRACT

Research under this grant used data from the Pacific Northwest Seismograph Network (PNSN) to study several aspects of earthquake hazards in the Pacific Northwest, including of two significant earthquake sequences, March 25, 1993 Scotts Mills, Oregon M 5.7 earthquake and the January 29, 1995 Robinson Point M 5.0 Puget lowland earthquake. Other research results under this grant include an investigation of the crustal structure beneath the Cascades, development of a method to accurately estimate earthquake moment from standard network data, and preliminary work on seismic wave velocity structure in the Puget Basin.

FINAL TECHNICAL REPORT
USGS NEHRP GRANT 1434-95-G-2597
Earthquake Hazard Research in the Pacific Northwest using Washington Regional Seismograph Network Data

Robert S. Crosson
University of Washington
GEOPHYSICS Box 351650
Seattle, WA 98195-1650
Phone:(206)543-6505 FAX:(206)543-0489 E-mail:crosson@u.washington.edu

Program Element: II.1

NON-TECHNICAL ABSTRACT

Research under this grant used data from the Pacific Northwest Seismograph Network (PNSN) to study several aspects of earthquake hazards in the Pacific Northwest, including of two significant earthquake sequences, March 25, 1993 Scotts Mills, Oregon M 5.7 earthquake and the January 29, 1995 Robinson Point M 5.0 Puget lowland earthquake. Other research results under this grant include an investigation of the crustal structure beneath the Cascades, development of a method to accurately estimate earthquake moment from standard network data, and preliminary work on seismic wave velocity structure in the Puget Basin.

TECHNICAL ABSTRACT

A. The March 25, 1993 Scotts Mills, Oregon earthquake sequence. We have carried out a detailed study of aftershocks and focal mechanisms of the March 25, 1993 Scotts Mills magnitude 5.7 crustal earthquake. The oblique thrust fault causing this earthquake strikes NW and is consistent with other NW striking faults in NW Oregon. Earthquakes as large as magnitude 6 present a hazard to the region. We have also found that ground motion variations are strongly affected by local geology in the vicinity of Scotts Mills.

B. Source Scaling for Regional Earthquakes We have completed work on the calibration of source moment scaling and station calibration for the Pacific Northwest Seismograph Network (PNSN). This research makes it possible to perform moment estimates more accurately using short period vertical component stations of the network.

C. The January 29, 1995 Robinson Point Puget lowland earthquake. A magnitude 5.0 earthquake occurred on 29 January, 1995 in the central Puget lowland at a depth of about 20 km. This earthquake was well recorded and located in the vicinity of the Seattle fault. We have analyzed the source characteristics of this event using broadband and short-period instrumental data. The fault slip producing this event is consistent with the deeper projections of the Seattle fault and it is possible that the earthquake represents tectonic deformation related to the Seattle fault system.

D. A cross-Cascades refraction profile using earthquake sources. We have completed earlier work on a cross-Cascade deep structure modeling, with results published in JGR. This research has revealed a deep crustal root of the Cascades which we interpret to be of mafic composition. The root is interpreted to be the result of crustal underplating.

E. Investigations of 3-D structure in the Puget lowland region. Under this research, we initiated efforts to obtain higher resolution P-wave velocity structure in the Puget Sound basin using earthquakes and explosions recorded on the PNSN. Toward this end, a tomographic inversion method is being implemented in which finite difference travel-time calculation is performed.

RESULTS

A. Scotts Mills Earthquake Sequence

A magnitude 5.7 crustal earthquake occurred on March 25, 1993 near the town of Scotts Mills, Oregon. This earthquake was centered in a sparsely populated region near the east side of the Willamette Valley, but was nevertheless somewhat damaging in Salem, Oregon. The mainshock was well recorded with the PNSN, and a significant aftershock sequence was well recorded on portable stations deployed following

the mainshock.

We analyzed a selected subset of 50 well recorded aftershocks in detail, computing high quality locations and first-motion focal mechanisms for these events. We conclude that the orientation of mainshock mechanism taken together with the aftershock distribution indicates that this event occurred as an oblique thrust on a northwest trending mid-crustal fault [Thomas, et al., 1996]. We tentatively associated this fault with the NW striking Mt. Angel fault which was studied most recently by Werner et al. [1992] in the vicinity of the Scotts Mills epicenters. The existence of a significant crustal fault in this region that has surface expression and can generate a M 5.7 earthquake at a depth of 15 km suggests that the Mt. Angel fault zone could possibly generate significantly larger earthquakes, in the magnitude 6 or greater range.

We are are preparing final revisions of manuscript describing the analysis of ground motion variations recorded in the Scotts Mills region during the aftershock deployment. In this work, we found significant relative site amplification effects, which we attribute to near-surface variations in geology.

B. Source Scaling for Regional Earthquakes

Accurate magnitude and moment estimation is an important aspect of regional network operation. Magnitudes and moments are fundamental characterizations of earthquake that are used in many other types of analysis. For example, fault slip rates and cumulative slip estimates may be made from moment estimates.

To improve our ability to estimate moments using regional network data (specifically, the PNSN data) we explore the use of scattered coda-wave amplitudes using the single scattering amplitude model of Aki and Chouet [1975]. This research led to a practical method which can be automated and incorporated into routine network data analysis. The method is described in Dewberry and Crosson [1995].

C. Robinson Point Earthquake

On January 29, 1995 an unusual magnitude 5.0 mid-crustal earthquake occurred in the southern Puget Sound lowland, between Seattle and Tacoma. The hypocenter of this event was located at about 20 km depth, and only a few sporadic aftershocks followed the mainshock. Although the event was widely felt in the Puget lowland, it was only slightly damaging as a result of its significant depth and location. P-wave first motions from the PNSN show that the mainshock was dominantly a thrust event with nearly east-west striking slip planes.

An empirical Green's function analysis using regional broadband stations indicates that this was a high stress-drop event (430 bars estimated [Dewberry and Crosson, 1996]). A small source region, consistent with the impulsive nature of the source, is also consistent with a tight pattern of epicenters for the few aftershocks that could be accurately located. Comparison with other regional earthquakes of comparable size indicates that earthquakes with hypocenters at depths greater than about 18 km in western Washington (and probably western Oregon) have anomalous aftershock sequences, with few, sporadic aftershocks. Although the reason for this behavior is not clear, it likely reflects temperature or compositional variation with depth.

The hypocenters of the Robinson Point sequence lie about 25 km south of the surface expression of the Seattle fault, an EW striking blind thrust extending across the center of the Puget Lowland. It is possible that the mainshock occurred on a basal extension of the Seattle fault, although uncertainty of the configuration of this fault at depth makes this possibility conjectural. If so, it would be the first direct seismological observation that the Seattle fault is active (although there is paleoseismic evidence of activity; e.g., Bucknam et al. [1992]). Further analysis of this earthquake may provide important insight on this possibility.

D. Cross-Cascade Profile

We have completed work on interpreting a cross-Cascades seismic refraction profile using earthquakes as sources rather than more conventional explosions [Schultz and Crosson, 1996]. In this work, we constructed a profile extending from the vicinity of Hood Canal in western Washington, across the Cascade Range to the vicinity of Walla Walla in southeastern Washington. We chose earthquakes and PNSN seismograph stations lying near the profile, so that a 2-D analysis could be carried out.

The most significant finding of this research is the discovery of seismic evidence for a crustal "root" beneath the Cascade Range. In the depth range between 35 km and 47 km, there is a distinct crustal root

that approximately mirrors the topographic profile of the Cascade Range. This root is interpreted as the result of localized magmatic underplating resulting from the release of volatiles in the process of dewatering of the Juan de Fuca slab during subduction. Ultimately, the mass redistribution resulting from underplating produces uplift as a result of isostatic readjustment. Geologic evidence suggest that this process has been enhanced in the past 5-7 m.y., bringing the Cascades to their present topographic prominence. Gravity data are generally consistent with isostatic equilibrium in the Cascade Range and support the seismic model. Our results are the first clear indication of a crustal root beneath the Cascades, and strongly indicate the general nature of late Cenozoic mountain building for the Cascades.

This research also demonstrates the utility of using regional seismograph network data for interpreting structure. When station and earthquake distributions permit, high resolution structure information may be obtained using natural sources.

E. 3-D Structure in the Puget Lowland

The Puget lowland produces the most intense non-localized distribution of small earthquakes in the Pacific Northwest. The recent attention focused on the Seattle fault [e.g., Bucknam et al., 1992] and the Seattle basin [Johnson et al., 1994], have made it clear that 1-D seismic structure may not be adequate for the location of crustal earthquakes in the Puget lowland, and also that earthquakes such as the Robinson Point event (see above) may possibly be related to the Seattle fault. To gain further insight into the relationship between small earthquakes and structure, we need (a) improved regional 3-D velocity structure models, and (b) to be able to use 3-D structure models effectively in locating and studying small and moderate earthquakes.

We have refined the basic finite difference method of Nelson and Vidale [1990] in order to efficiently locate earthquakes in a general 3-D velocity medium. Our refinements include some changes to the finite difference algorithm itself, and refinements in the way grid search is done to make the process more efficient. In the course of this development, we discovered that many earthquakes in the vicinity of the Seattle fault produce double minima in their residual functions, making depth determination problematic. This problem may be worsened by strong lateral velocity variations which we know exist in the central Puget lowland. We are continuing to investigate this problem to resolve possible ambiguities in depth.

The second major objective is to achieve a practical, usable 3-D velocity structure for the Puget lowland and vicinity. We have developed a grid parameterization which allows flexible modeling of diverse input data, including earthquake and explosion travel times. As a first step in the full joint inversion of velocity and hypocenters, we are constructing a model of the Puget lowland using existing refraction/wide-angle reflection models along profile lines and a previous linear tomographic inversion as constraints. This initial reference model allows us to compare different model interpretation for consistency in regions where they intersect. After evaluation, these models will be used as weighted constraints in the general inversion problem.

References

Aki, K. and B. Chouet, Origin of coda waves: source, attenuation and scattering effects, JGR, V. 74, pp. 615-631, 1975.

Bucknam, R.C., E. Hemphill, and E.B. Leopold, Abrupt uplift within the past 1700 years at southern Puget Sound, Washington, Science, 258, 1611-1614, 1992.

Dewberry, S. R., and R. S. Crosson, Source scaling and moment estimation for the Pacific Northwest Seismograph Network using S-coda amplitude, Bull. Seis. Soc. Am., 85, 1309-1326, 1995.

Dewberry, S. R., and R. S. Crosson, The M_D earthquake of 29 January 1995 in the Puget Lowland of western Washington: an event on the Seattle fault?, BSSA, V. 86, N. 4, pp. 1167-1172, 1996.

Johnson, S.Y, C.J. Potter, and J.M. Armentrout, Origin and evolution of the Seattle fault and Seattle basin, Geology, 22, 71-74, 1994.

Nelson, G.D., and J. Vidale, Earthquake locations by 3-D finite-difference travel times, Bull. Seis. Soc. Am., 80, 395-410, 1990.

Thomas. G.C., R. S. Crosson, D. L. Carver and T. S. Yelin, The 25 March 1993 Scotts Mills, Oregon earthquake and aftershock sequence: Spatial distribution, focal mechanisms, and the Mt. Angel Fault, BSSA, V. 86, N. 4, pp. 925-935, 1996.

Thomas, G. C., and R. S. Crosson, Site effects near Scotts Mills, Oregon using S-wave data, (accepted and in final revision for Geophys. Res. Lett.).

Werner, K., J. Nabelek, R. Yeats, and S. Malone, The Mt. Angel fault: Implications of seismic-reflection data and the Woodburn, Oregon, earthquake sequence of August, 1990, Oregon Geology, 54, 112-117, 1992.

APPENDIX 1

Publications wholly or partially funded under this grant

Articles

Dewberry, S. R., and R. S. Crosson, Source scaling and moment estimation for the Pacific Northwest Seismograph Network using S-coda amplitude, Bull. Seis. Soc. Am., 85, 1309-1326, 1995.

Dewberry, S. R., and R. S. Crosson, The M_D earthquake of 29 January 1995 in the Puget Lowland of western Washington: an event on the Seattle fault?, BSSA, V. 86, N. 4, pp. 1167-1172, 1996.

Ma, L., R. S. Crosson, and R. S. Ludwin, Focal mechanisms of western Washington earthquakes and their relationship to regional tectonic stress, In: Assessing earthquake hazards and reducing risk in the Pacific Northwest; Volume 1.; A.M. Rogers, T.J. Walsh W.J. Kockelman and G.R. Priest, editors; U.S. Geological Survey Professional Paper; U.S. Geological Survey. Reston, VA, United States; pp 257-283, 1996.

Schultz, A. P., and R. S. Crosson, Seismic velocity profile across the central Washington Cascade Range from refraction interpretation with earthquake sources, JGR (B), V. 101, N.12, pp. 27,899-27,915, 1996.

Thomas, G.C., R. S. Crosson, D. L. Carver and T. S. Yelin, The 25 March 1993 Scotts Mills, Oregon earthquake and aftershock sequence: Spatial distribution, focal mechanisms, and the Mt. Angel Fault, BSSA, V. 86, N. 4, pp. 925-935, 1996.

Thomas, G. C., and R. S. Crosson, Site effects near Scotts Mills, Oregon using S-wave data, (accepted and in final revision for Geophys. Res. Lett.).

Theses

Dewberry, Shawn Robert, Crustal and upper mantle structure for the Pacific Northwest from an analysis of short-period Teleseismic Network Data, Ph.D. Dissertation, Geophysics Program, University of Washington, Seattle, Washington, 166 p., 1996

Abstracts

Crosson, R.S., and S.R. Dewberry, Receiver function estimation from short-period regional network teleseismic data using cepstral deconvolution, EOS, 75, p. 485, 1994.

Dewberry, S.R., and R.S. Crosson, Comparison of stacking and cepstral deconvolution in estimation of receiver functions from short-period regional network teleseismic data, EOS, 75, p. 485, 1994.

Symons, N.P., and R. S. Crosson, Relocation of earthquakes in the Puget lowland thrust sheet, Seis. Res. Lett., 66, p. 47, 1995.

Symons, N.P., and R. S. Crosson, Construction of 3-D velocity model for the Puget Sound region using heterogeneous data, EOS, 76, p. F402, 1995.

Thomas, G.C., and R. S. Crosson, Calibrating coda duration magnitudes in the Pacific Northwest, EOS, 76, p. F424, 1995.

Thomas, G.C., and R. S. Crosson, Corner frequency analysis of aftershocks following the 25 March 1993, Scotts Mills, Oregon, earthquake, Seis. Res. Lett., 66, p. 47, 1995.

APPENDIX 2

The M_D 5.0 Earthquake of 29 January 1995 in the Puget Lowland of Western Washington: An Event on the Seattle Fault?

by Shawn R. Dewberry and Robert S. Crosson

Abstract   The magnitude M_D = 5.0 Robinson Point earthquake occurred on 29 January 1995 at 03:11 UTC approximately 25 km south of Seattle, Washington. We investigate the single foreshock, the mainshock, and the weak aftershock sequence using short-period and broadband data recorded by the Pacific Northwest Seismograph Network. P-wave first motions from the mainshock indicate reverse faulting with east–west trending nodal planes. Aftershock epicenters cluster about the mainshock with aftershock hypocenters exhibiting a nearly vertical distribution, possibly an effect of depth error. The mainshock, at a depth of 19.6 km, is the deepest event in the sequence. An empirical Green's function analysis indicates that the mainshock source time function (STF) is impulsive with a 0.3- to 0.4-sec duration. A minimum stress drop of 430 bars is inferred, identifying this as a high-stress-drop event. Comparison with five other moderate-sized Pacific Northwest mainshock-aftershock sequences suggests that mainshocks with depths greater than about 18 km have few, relatively small aftershocks that are confined to small source regions.

Introduction

On 29 January 1995 at 03:11:22 UTC, a magnitude 5 earthquake occurred near Robinson Point on Maury Island in Puget Sound, Washington. Using Pacific Northwest Seismograph Network (PNSN) data, the location of this event is 47.38° N, 122.35° W, with a depth of 19.6 km. The epicenter is approximately mid-way between the cities of Seattle and Tacoma. A coda duration magnitude (M_D) of 5.0 was estimated from short-period PNSN data. The National Earthquake Information Center reported magnitudes of m_b = 5.1 and M_S = 4.5, while the Pacific Geoscience Centre in Sidney, British Columbia, reported a magnitude of M_L = 4.9. Shaking was felt throughout western Washington and as far away as Salem, Oregon, and Vancouver, British Columbia. Minor damage was reported in Auburn and Tacoma, Washington. The mainshock was the largest crustal earthquake to occur in the Puget-Willamette lowland region of the Pacific Northwest since the M_L = 5.7 Scotts Mills earthquake of 25 March 1993 (Thomas et al., 1996). Figure 1 shows the locations of the Robinson Point mainshock, five other moderate-sized crustal earthquakes (4.9 ≤ M ≤ 5.7) discussed below, and both short-period and broadband stations of the PNSN.

The Robinson Point sequence includes one foreshock (M_D = 2.1), the mainshock, and 28 aftershocks recorded through June 1995. This sequence is noteworthy for the following reasons. The mainshock was the first moderate-sized ($M \gtrsim 5$) Puget Sound earthquake to be recorded by the three-component, wide dynamic range, broadband instruments

recently added to the PNSN. This broadband data provides the only unclipped relatively near-field records of the mainshock recorded on high-sensitivity stations. Also, the small number of aftershocks indicates that this is an anomalous mainshock-aftershock sequence compared with other Pacific Northwest crustal earthquakes.

The relation of the Robinson Point sequence to the Seattle Fault is of particular interest. The Seattle Fault (Johnson et al., 1994) is an east–west trending, blind, reverse fault that dips to the south steeply at the surface and possibly more gradually at depth. The inferred surface expression of this fault is approximately 25 km north of the mainshock epicenter (see Fig. 2a). Surface geologic observations suggest that reverse slip occurred on the Seattle Fault 500 to 1700 yr ago (Bucknam et al., 1992), producing an earthquake as large as magnitude 7. Recent interpretation of Puget Sound structures at depth from industry reflection data (Pratt et al., 1994) indicates that the Robinson Point earthquake could be located on the basal extent of the Seattle Fault.

Network Data Analyses and Discussion

Magnitudes and Locations

Magnitudes for the sequence were calculated using the coda duration formula of Crosson (1972), modified to incorporate median (rather than mean) durations for more robust results. Resulting M_D values for the sequence range from 0.8 to 5.0, with the largest aftershock of M_D = 2.4.
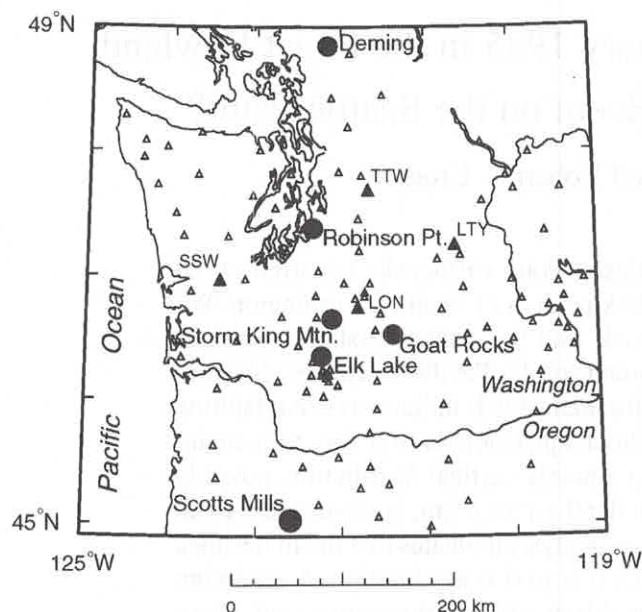
Figure 1.   Map of the Pacific Northwest showing the short-period (open triangles) and broadband, three-component (filled triangles) stations of the PNSN. Epicenters of six moderate-sized earthquakes (circles), including the Robinson Point earthquake, are also shown.

Initial locations for this sequence were determined using the 1D reference layered velocity model used by Lees (1989). Following the station residual analysis procedure described by Lees (1989), we added station corrections for six stations that were not previously available. From the data set of 30 earthquakes, high-quality locations were determined for a subset of 17 events using a minimum of 13 P arrivals (including the two closest stations SPW and MEW) and a maximum azimuthal gap of 100°. Only stations within 200 km of the epicenters were used in the location calculations. These well-located events had epicenters that cluster within 2 km of the mainshock, with no obvious lateral alignment or trend. Aftershock hypocenter depths tended to be shallower than the mainshock depth.

To reduce the relative error in the hypocenter locations, the 17 high-quality events were relocated using modified station corrections set to reduce the mainshock residuals to zero. Thus, the mainshock was used as a master event. Figure 2a shows the epicenters after relocation, and Figure 2b is a cross section along A-A′ showing the relocated hypocenters. The depths have a 3.7-km range with all hypocenters in a nearly vertical distribution. The 95% confidence interval for the depth uncertainties is approximately 2 km, so the vertical spread in depth may be mostly explained by depth error.

Focal Mechanisms

Of the 17 well-located events in the sequence, only the foreshock and mainshock provided adequate data for well-
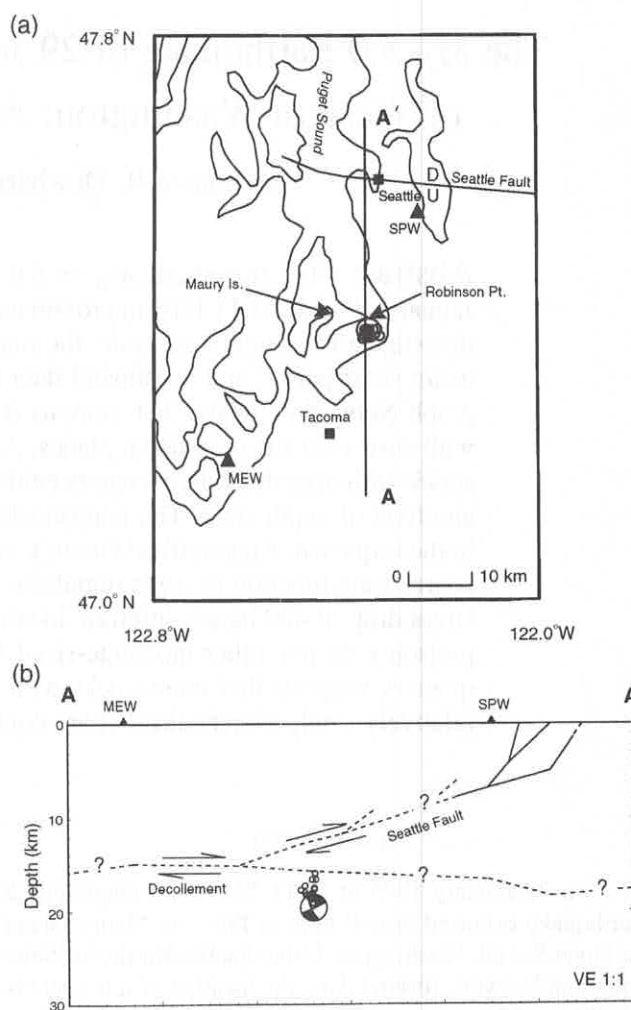

Figure 2.   (a) Epicenter locations for 17 well-located events relocated using a master event relocation scheme. PNSN short-period stations SPW and MEW are displayed along with the surface projection of the Seattle Fault. (b) The relative hypocenter distribution for the events in (a) projected onto a cross section along the profile (A-A′) shown in (a). Projections of the Seattle Fault and Puget thrust sheet decollement, as proposed by Pratt et al. (1994), are also shown (T. Pratt, personal comm., 1995). Inferred structure is shown with dashed lines. Relative motions across each structure are noted with arrows. The vertical exaggeration is 1:1.

constrained P-wave first-motion focal mechanisms. The mainshock has a predominantly reverse fault focal mechanism. The mechanism solutions are quite stable when determined for a range of hypocenter depths that span the depth uncertainty. The foreshock and mainshock mechanisms are as follows: (strike, dip, rake) 80°, 35°, 90° and 95°, 25°, 110°. Equal-area, lower-hemisphere projections of each focal mechanism are given in Figure 3. The P-axis orientations for both mechanisms trend north–south (azimuth = 350°) with shallow plunges (10° to 21°). These are consistent with
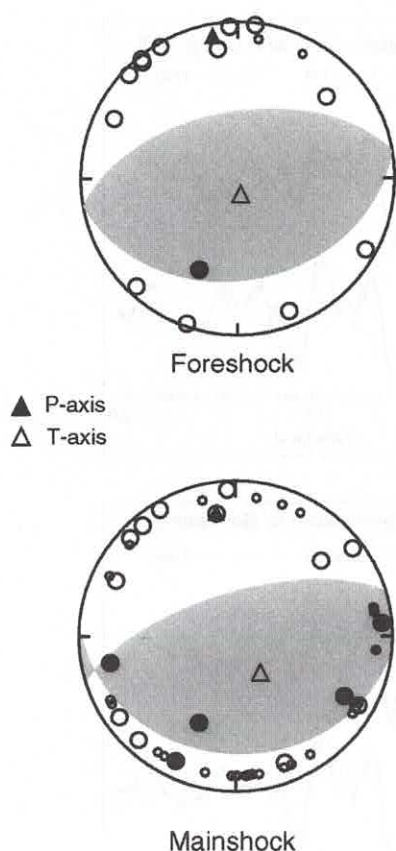
Foreshock

▲ P-axis
△ T-axis

Mainshock

Figure 3. Foreshock and mainshock fault-plane solutions as determined from *P*-wave first motions. Compressional first motions are displayed with filled circles. Stations with upgoing rays are displayed with the larger symbols. Both solutions are plotted using equal-area, lower-hemisphere projections.

orientations found for other Puget Sound region crustal earthquakes (e.g., Ma *et al.*, 1991). Moment-tensor analysis of regional broadband data from 10 stations in Washington, Oregon, and British Columbia gives a similar thrust mechanism for the mainshock and a comparable depth of 18 km (J. Nábelek, personal comm., 1995). The correct slip plane clearly cannot be ascertained from the aftershock distribution alone.

We examined the proposed structural model of Pratt *et al.* (1994) in conjunction with the sequence hypocenters and the focal mechanisms. Included in the cross section of Figure 2b are the projections (onto the profile A-A′) of the Seattle Fault and detachment structure (decollement) as proposed by Pratt *et al.* (1994). Their model is derived from industry reflection data with depth resolution to 10 to 12 km. As shown in Figure 2b, the sequence hypocenters lie at or below the inferred structural interfaces of the Pratt *et al.* (1994) model. Although the focal mechanism nodal planes are easier to reconcile with the deep extension of the Seattle Fault as modeled, the uncertainties in both their structural model and the hypocenters cannot preclude other possible fault

structures, such as the decollement, a conjugate to the Seattle Fault, or an unrelated fault. Clearly, no definitive answer can be drawn from this sequence alone. The need for improved structural constraint at hypocentral depths in this region is evident.

Empirical Green's Function Analysis

Broadband waveforms from the mainshock and single foreshock were used in an empirical Green's function (EGF) deconvolution (Mueller, 1985) to estimate the mainshock source time function (STF). This is a well-established technique used recently by other investigators analyzing body waves at local and regional distances (e.g., Nábelek and Xia, 1995). A good estimate of the true mainshock STF should result so long as the EGF signal-to-noise ratio is adequate and the reference event is small relative to the main event.

The $M_D = 2.1$ foreshock, with a focal mechanism and location similar to the mainshock, was used as an EGF. A water-level deconvolution (Helmberger and Wiggins, 1971) was performed using data from the only broadband station with adequate signal to noise that recorded both events, station LON (see Fig. 1 for station location). Estimates for the mainshock STF were first derived independently from radial (R)- and vertical (Z)-component waveforms windowed about the *P* arrival (Fig. 4a). A single pulse of duration 0.3 to 0.4 sec resulted from the deconvolution of each component. These STFs were reconvolved with the reference event waveforms and compared with the observed mainshock waveforms to qualitatively assess the EGF deconvolution performance. The predicted R-component waveform modeled the observed waveform well, while the predicted Z-component waveform poorly fit the observed data. Substituting a simple gaussian pulse of duration 0.4 sec (Fig. 4b) for the STF estimates maintained agreement between the R-component waveforms, as before, while improving the fit of the Z-component waveform. A similar improvement was seen when the R-component STF was substituted for the Z-component STF. From qualitative comparisons between predicted and true waveforms using both the R-component and gaussian pulse STFs (Figs. 4c and 4d), the final STF estimate is determined to be a simple pulse of duration 0.3 to 0.4 sec (Fig. 4b).

Assuming a rupture velocity of 3.0 km/sec (0.8 V_S), the above source duration corresponds to a rupture length of 0.9 to 1.2 km. We calculated the stress drop using the Brune (1970, 1971) source model

$$\Delta\sigma = \frac{7M_0}{16r^3},$$

where $\Delta\sigma$ is the stress drop, M_0 is the seismic moment, and r is the source radius. Using a moment value of 2.13×10^{23} dyne-cm (J. Nábelek, personal comm., 1995) and a fault radius of 0.6 km gives a minimum stress drop of 430 bars. A high-stress-drop designation is indicated for this event. For comparison, Nábelek and Xia (1995) found a source
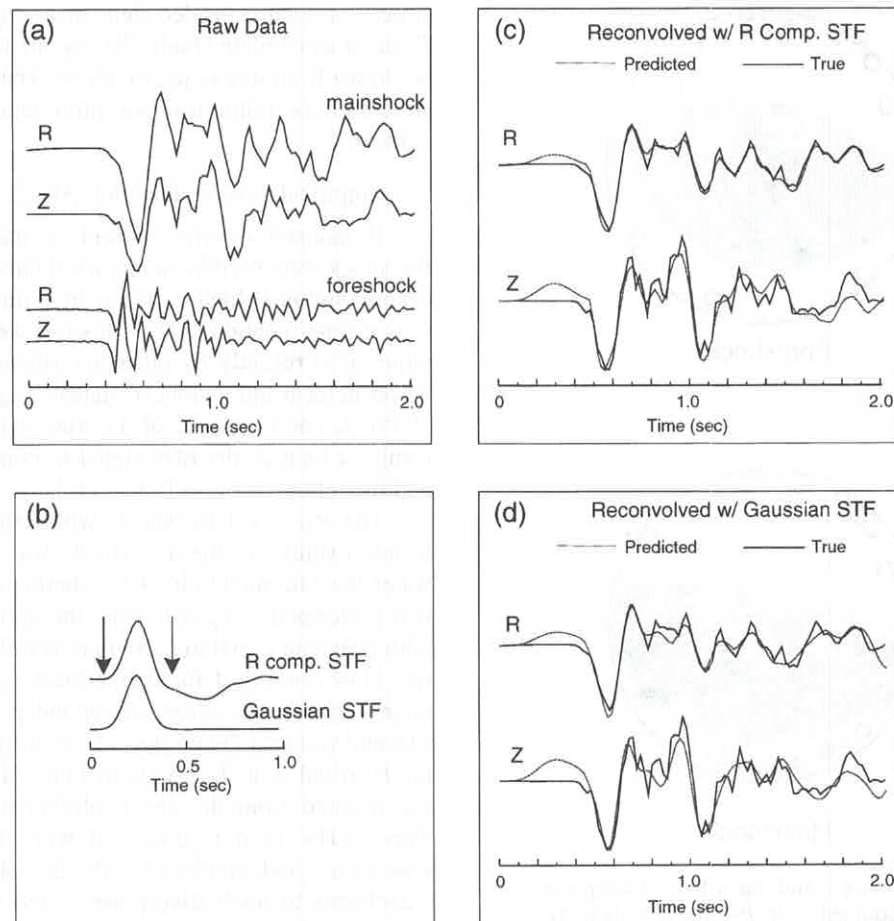
Figure 4.   (a) Raw radial and vertical P waveforms for the mainshock and foreshock recorded at station LON. (b) Mainshock STF estimates from the radial-component EGF deconvolution and a simple gaussian pulse. The pulse duration is delimited by the two arrows. (c) Comparisons of the true and predicted data for each component using the radial-component STF from (b). (d) Comparisons of the true and predicted data for each component using the gaussian pulse STF from (b).

duration of 1.8 sec and a stress drop of approximately 40 bars for the $M_L = 5.7$ Scotts Mills mainshock.

Comparison with Other Earthquakes

The Robinson Point mainshock-aftershock sequence is unusual due to its small and irregular sequence of aftershocks and absence of larger aftershocks (Fig. 5). To determine whether this behavior is anomalous with respect to other regional earthquakes, we compared the Robinson Point aftershock sequence with aftershock sequences of five other moderate-sized, crustal earthquakes that were well recorded by the PNSN. These sequences are associated with the 1981 Elk Lake (Grant et al., 1984; Atkinson, 1995), 1981 Goat Rocks (Zollweg and Crosson, 1981), 1990 Deming (Qamar and Zollweg, 1990; Atkinson, 1995; Dewberry and Crosson, 1995), 1993 Scotts Mills (Nábelek and Xia, 1995; Thomas et al., 1996), and 1989 Storm King Mountain (Atkinson, 1995) earthquakes. The mainshock epicenters are shown in

Figure 1. A summary of event parameters for all six mainshocks is given in Table 1. Time histories for the first 100 days of all six sequences are shown in Figure 5. The time histories of the sequences associated with the four shallowest mainshocks (Elk Lake, Goat Rocks, Deming, and Scotts Mills) exhibit two similar characteristics. First, each has a significant number of aftershocks (70 to 600 events) above $M_D = 0.0$. Second, the frequency of occurrence shows an exponential decay with time. In contrast, the time histories for the two aftershock sequences following the deepest mainshocks (Storm King Mountain and Robinson Point) show relatively few aftershocks (<30 events) with no clear decay in aftershock occurrence rate or magnitude in the time period immediately following the mainshock. In addition, both the Storm King Mountain and Robinson Point sequences show an absence of events with $M_D > 2.4$ (Fig. 5). Noting that both mainshock epicenters are centrally located within the PNSN where detection and location capabilities

Elk Lake

Z = 6.7km

y-axis: Magnitude (M_D)
x-axis: Time (days after main)

Goat Rocks

Z = 3.2km

y-axis: Magnitude (M_D)
x-axis: Time (days after main)

Deming

Z < 5.0km

y-axis: Magnitude (M_D)
x-axis: Time (days after main)

Scotts Mills

Z = 15.1km

y-axis: Magnitude (M_D)
x-axis: Time (days after main)

Storm King Mtn.

Z = 18.4km

y-axis: Magnitude (M_D)
x-axis: Time (days after main)

Robinson Point

Z = 19.6km

y-axis: Magnitude (M_D)
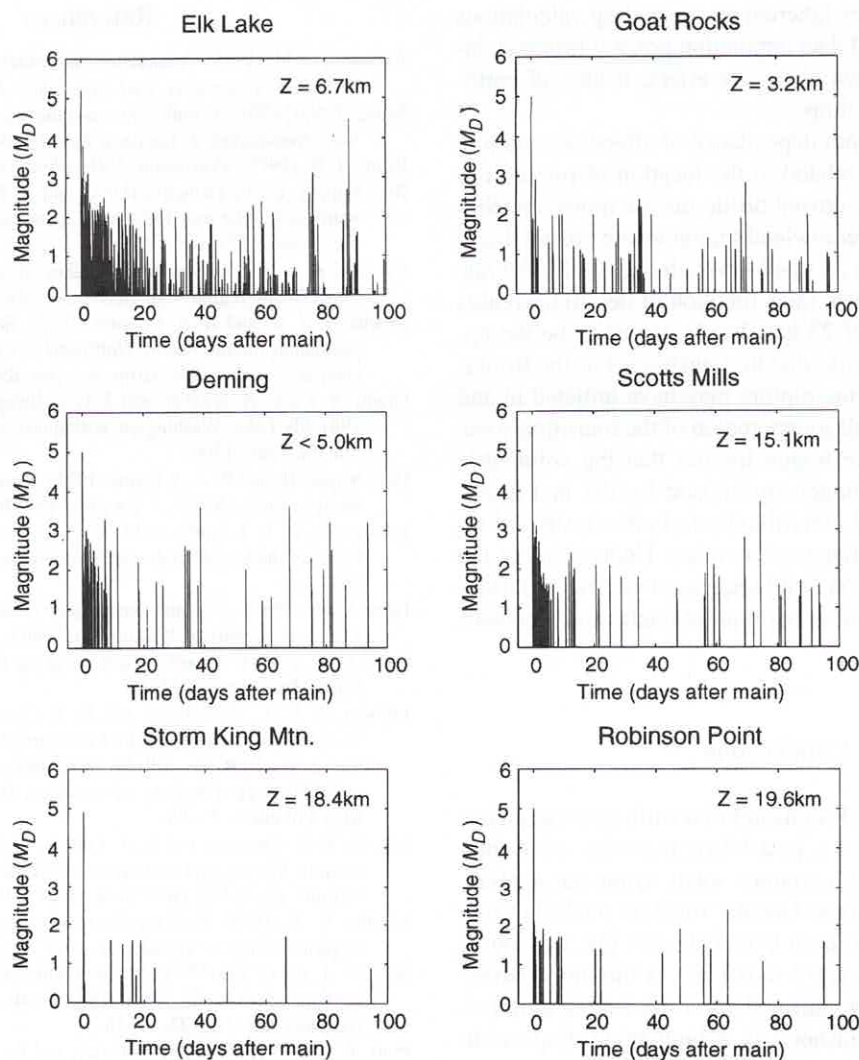*x-axis:* Time (days after main)

Figure 5.   Time-magnitude plots for six selected Pacific Northwest aftershock sequences, including all events with $M_D > 0.0$ within an 18-km radius of the mainshock epicenter. Mainshock depths are noted.

Table 1
Location Information for Selected Moderate-Sized, Crustal Earthquakes Occurring in Western Washington and Oregon

Approx. Location	Date (mm dd yy)	Time UTC (hr:min:sec)	Lat. (°N)	Lon. (°W)	Depth (km)	M_D	M_L	$\Delta\sigma$ (bars)
Elk Lake	02 14 1981	06:09:27.3	46.350	122.244	6.7	5.2	5.5	10–111
Goat Rocks	05 28 1981	09:10:45.9	46.525	121.394	3.2	5.0	5.0	—
Storm King Mtn.	12 24 1989	08:45:58.9	46.650	122.116	18.4	4.9	5.1	50
Deming	04 14 1990	05:33:26.6	48.845	122.160	<5.0	5.0	5.2	25–32
Scotts Mills	03 25 1993	13:34:35.9	45.032	122.586	15.1	5.6	5.7	40
Robinson Point	01 29 1995	03:11:22.7	47.383	122.350	19.6	5.0	—	430

are optimal, the lack of aftershocks is doubtfully an artifact of detection capability.

The stress-drop values listed in Table 1 show that the deepest mainshocks (Robinson Point and Storm King Mountain), which occurred within the lower portion of the crustal seismogenic zone in the Puget lowland (Ludwin *et al.*, 1991), are associated with larger stress drops as well as fewer aftershocks, though the data population is relatively small. While the observations suggest that aftershock behavior and mainshock stress drop may be dependent on mainshock

depth, the uncertainties inherent in stress-drop calculations coupled with the small data population prevent firm conclusions from being drawn about the effect, if any, of earthquake depth on stress drop.

The suggested depth dependence of aftershock number and behavior may be related to the location of rupture nucleation relative to the crustal brittle-ductile transition (Sibson, 1982). In the Puget lowland region where crustal thickness is estimated to be 35 to 40 km (Schultz, 1993), the rate of earthquake occurrence (as a function of depth) decreases rapidly near a depth of 25 km. We infer this to be the approximate depth of brittle-ductile transition. For the Robinson Point mainshock, the rupture may have initiated in and been confined to a small source region of the transition zone. The small-sized source region implies that the volumetric extent of stress inhomogeneity created by the mainshock rupture was also small, contributing to both a restricted aftershock region and aftershock number. Understanding the behavior of the Robinson Point sequence may lead to further insight into the behavior of earthquake nucleation processes at mid-crustal depths.

Conclusions

Association of the Robinson Point earthquake sequence with the Seattle Fault is a possibility; however, we cannot resolve this issue with certainty solely from the analysis completed here. Empirical Green's function analysis using broadband data from station LON indicates that the source time function duration is 0.3 to 0.4 sec. A minimum stress-drop value of 430 bars, inferred from the source duration, indicates that the mainshock is a high-stress-drop earthquake.

The weak aftershock sequence that followed is similar in nature to that of another mid-crustal event, the 1989 Storm King Mountain earthquake. These two aftershock sequences are markedly different from the sequences associated with four other moderate-sized Pacific Northwest crustal events with shallow ($z < 18$ km) hypocenter depths. The observed differences in the aftershock behavior and mainshock stress drops suggests a depth dependence for the aftershock behavior of crustal earthquakes in the Pacific Northwest.

Acknowledgments

References

Atkinson, G. M. (1995). Attenuation and source parameters of earthquakes in the Cascadia region, Bull. Seism. Soc. Am. 85, 1327–1342.
Brune, J. N. (1970). Tectonic stress and the spectra of seismic shear waves from earthquakes, J. Geophys. Res. 75, 4997–5009.
Brune, J. N. (1971). Correction, J. Geophys. Res. 76, 5002.
Bucknam, R. C., E. Hemphill-Haley, and E. B. Leopold (1992). Abrupt uplift within the past 1700 years at southern Puget Sound, Washington, Science 258, 1611–1614.
Crosson, R. S. (1972). Small earthquakes, structure, and tectonics of the Puget Sound region, Bull. Seism. Soc. Am. 62, 1133–1171.
Dewberry, S. R. and R. S. Crosson (1995). Source scaling and moment estimation for the Pacific Northwest seismograph network using S-coda amplitudes, Bull. Seism. Soc. Am. 85, 1309–1326.
Grant, W. C., C. S. Weaver, and J. E. Zollweg (1984). The 14 February 1981 Elk Lake, Washington, earthquake sequence, Bull. Seism. Soc. Am. 74, 1289–1309.
Helmberger, D. and R. A. Wiggins (1971). Upper mantle structure of midwestern United States, J. Geophys. Res. 76, 3329–3345.
Johnson, S. Y., C. J. Potter, and J. M. Armentrout (1994). Origin and evolution of the Seattle fault and Seattle basin, Washington, Geology 22, 71–74.
Lees, J. M. (1989). Seismic tomography in western Washington, Ph.D. Thesis, University of Washington, Seattle, 173 pp.
Lees, J. M. (1995). Xmap8: a free program for three-dimensional GIS, Seism. Res. Lett. 66, 33–37.
Ludwin, R. S., C. S. Weaver, and R. S. Crosson (1991). Seismicity of Washington and Oregon, in Neotectonics of North America, D. B. Slemmons, E. R. Engdall, M. D. Zoback, and D. D. Blackwell (Editors), Geological Society of America, Boulder, Colorado, Decade Map Volume 1, 77–98.
Ma, L., R. S. Crosson, and R. S. Ludwin (1991). Focal mechanisms of western Washington earthquakes and their relationship to regional tectonic stress, U.S. Geol. Surv. Open-File Rept. 91-441-D.
Mueller, C. S. (1985). Source pulse enhancement by deconvolution of an empirical Green's function, Geophys. Res. Lett. 12, 33–36.
Nábelek, J. and G. Xia (1995). Moment-tensor analysis using regional data: applications to the 25 March, 1993, Scotts Mills, Oregon, earthquake, Geophys. Res. Lett. 22, 13–16.
Pratt, T. L., S. Y. Johnson, C. J. Potter, and W. J. Stephenson (1994). The Puget lowland thrust sheet (abstract), EOS 75, 621.
Qamar, A. and J. Zollweg (1990). The 1990 Deming Washington earthquake: a sequence of shallow thrust earthquakes in the Pacific Northwest (abstract), EOS 71, 1145.
Schultz, A. P. (1993). A 2-D velocity structure for a cross-Cascades profile using earthquake sources, Master's Thesis, University of Washington, Seattle, 55 pp.
Sibson, R. H. (1982). Fault zone models, heat flow, and the depth distribution of earthquakes in the continental crust on the United States, Bull. Seism. Soc. Am. 72, 151–163.
Thomas, G. C., R. S. Crosson, D. Carver, and T. S. Yelin (1996). The 25 March 1993 Scotts Mills, Oregon earthquake and aftershock sequence: spatial distribution, focal mechanisms, and the Mount Angel Fault, Bull. Seism. Soc. Am. 86, 925–935.
Zollweg, J. E. and R. S. Crosson (1981). The Goat Rocks Wilderness, Washington earthquake of 28 May 1981 (abstract), EOS 62, 966.

University of Washington
Geophysics Program
Box 351650
Seattle, Washington 98195-1650

The 25 March 1993 Scotts Mills, Oregon, Earthquake and Aftershock Sequence: Spatial Distribution, Focal Mechanisms, and the Mount Angel Fault

by G. C. Thomas, R. S. Crosson, D. L. Carver, and T. S. Yelin

Abstract The 25 March 1993 $M_L = 5.7$ crustal earthquake near Scotts Mills, Oregon, was the largest earthquake to occur in the Pacific Northwest in over a decade. The mainshock was located at 45.033° N, 122.586° W and at a depth of about 15.1 km, based on arrival time data from the short-period Pacific Northwest Seismograph Network. Beginning about 12 h after the mainshock, investigators from the U.S. Geological Survey deployed 22 digital seismographs to record aftershocks. Using data from the temporary and permanent stations, we analyzed a subset of 50 after-shocks with quality locations. Hypocenters of these aftershocks lie on a northwest-trending steeply dipping plane (strike 290 ± 10°, dipping 60 ± 5° to the north-northeast), in agreement with the preferred slip plane of the mainshock focal mechanism solution (strike 294°, dipping 58° to the north-northeast). The planar structure defined by the aftershock locations may be a southeast continuation of the Mount Angel Fault, a reverse fault identified from both surface and subsurface evidence. The mapped southeast extent of the Mount Angel Fault is located less than 10 km west of the Scotts Mills epicentral region. In addition, the mainshock focal mechanism solution, with a combination of reverse motion and right-lateral strike slip, has a geometry and sense of motion consistent with the Mount Angel Fault. While aftershock focal mechanisms are varied, P axes are consistently oriented in a subhorizontal north–south direction. This earthquake sequence, together with the geological and geophysical evidence for the Mount Angel Fault, suggests a significant crustal earthquake hazard for this region of northwest Oregon.

Introduction

The Scotts Mills mainshock occurred on 25 March 1993, at 5:34 a.m. PST (13:34 UT), with $M_L = 5.7$ and coda duration magnitude $(M_D) = 5.6$. This was the largest earthquake to occur in the Pacific Northwest since the $M_L = 5.5$ Elk Lake earthquake of 14 February 1981 (e.g., Grant et al., 1984) and the $M_L = 5.0$ Goat Rocks earthquake of 28 May 1981 (Zollweg and Crosson, 1981). It has since been followed by the M 5.9 and M 6.0 earthquakes of 20 September 1993 near Klamath Falls in southern Oregon (e.g., Braunmiller et al., 1995). Figure 1 shows the location of the Scotts Mills mainshock and other important crustal (North America plate) earthquakes in the Pacific Northwest. Using 93 P-phase arrivals recorded by the Pacific Northwest Seismograph Network (PNSN; described by Ludwin et al., 1994), the Scotts Mills mainshock epicenter has been located at 45.033° N, 122.586° W with a focal depth of 15.1 km. Ground motion was felt in both the Willamette Valley and Puget Basin, from Roseburg, Oregon, to the south, to as far north as Seattle, Washington (Dewey et al., 1994). Peak hor-

izontal ground accelerations of 0.06 and 0.03 g were recorded at distances of 44 and 53 km, respectively (Dewey et al., 1994). Madin et al. (1993) estimate the total property damage at over $28 million. No evidence of surface faulting was reported.

Historic seismicity in northwest Oregon has been concentrated in the northern Willamette Valley, between Salem and Portland (e.g., Ludwin et al., 1991). Figure 2 shows a map of background seismicity for 1982–1992 for the Salem-Portland region. The Scotts Mills region, about 56 km south of Portland, is located near the southern boundary of seismic activity in western Oregon. Earthquakes in Portland have been interpreted to be related to one or more northwest-trending faults including the Portland Hills Fault (Yelin and Patton, 1991). Along the Portland Hills Fault, earthquakes with magnitudes as large as 3.5 have been observed to have focal mechanisms with a mixture of reverse and right-lateral strike-slip motion (Yelin, 1992). However, correlations of Portland earthquakes with individual faults is problematic
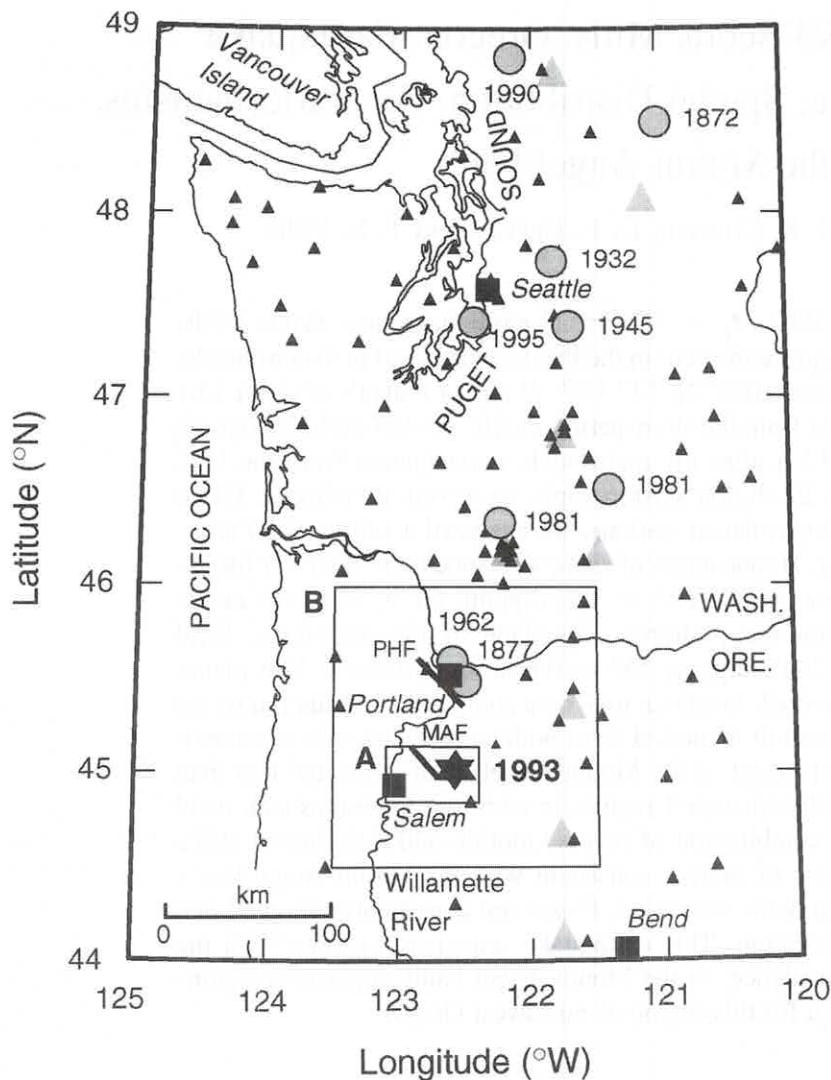
Figure 1. Map of western Washington and northwest Oregon featuring historic North America plate earthquakes of magnitude 5.0 or greater (circles), the Scotts Mills mainshock (star), PNSN seismographs operating in 1993 (solid triangles), and Quaternary volcanoes (gray triangles). PHF is the Portland Hills Fault, and MAF is the Mount Angel Fault. We refer to the area enclosed in box A as the Scotts Mills region, and the area enclosed in box B as the Salem–Portland region.

because the earthquakes are relatively deep (10–20 km) and the known faults lack evidence of recent surface displacement. Portland has experienced two moderate earthquakes: one of Modified Mercalli Intensity VII in 1877 (Thenhaus, 1978), and an M 5.2 in 1962 (Dehlinger et al., 1963; Yelin and Patton, 1991).

There were no observed foreshocks to the Scotts Mills earthquake, but in 1990, several small ($M \approx 2$) earthquakes occurred approximately 20 km northwest of the Scotts Mills epicenter, near Woodburn, Oregon (see also Werner et al., 1992). Figure 3 shows a map of epicenters of the Scotts Mills mainshock and 147 locatable aftershocks, as well as epicenters of earlier earthquakes including the Woodburn events of 1990. The Scotts Mills aftershock epicentral region is located about 10 km east of the most southeasterly mapped extent of the Mount Angel Fault.

The Mount Angel Fault (MAF) is part of the Gales Creek–Mount Angel lineament, a major northwest-trending structural zone that parallels the Portland Hills–Clackamas

River structural zone (Beeson et al., 1985, 1989) lying approximately 50 km to the north. The inferred surface trace of the MAF is shown in Figure 3. The MAF, with a mapped length of approximately 25 km, is primarily a subsurface reverse fault, dipping to the northeast (Werner et al., 1992). Hampton (1972) first mapped the southeast portion of the fault based on vertical offsets of Miocene flows of the Columbia River Basalt group found in outcrops and water wells. Hampton's (1972) mapped northwest extent of the MAF was roughly midway between Woodburn and Mount Angel. Additional well studies and seismic reflection profiles indicate that the fault extends northwest, to approximately 4 km northwest of Woodburn (Werner et al., 1992). The Miocene basalts have vertical displacements of up to 250 m, while the overlying Miocene and Pliocene fluvial and lacustrine sediments have offsets of approximately 100 m (Werner et al., 1992). This differential offset suggests continuing post-Miocene displacement across the fault. The offsets and dips of individual flows in the Columbia River Basalt group,
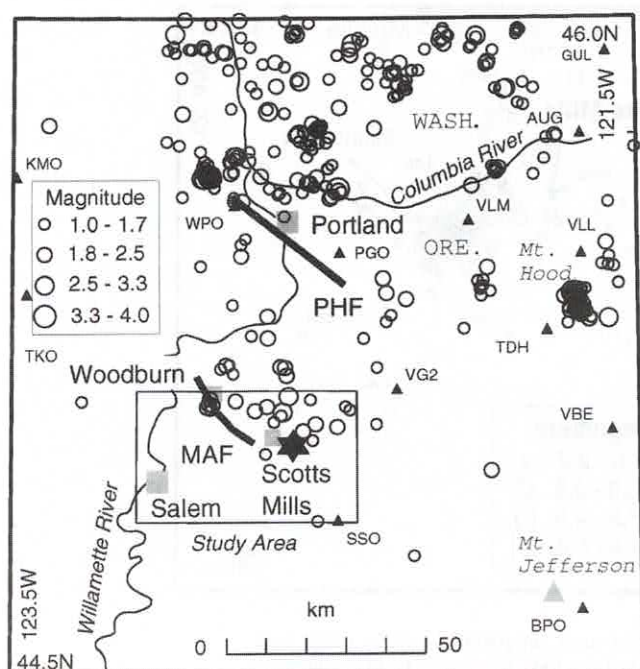
Figure 2. Background seismicity of the Salem–Portland region, 1982 through 1992. Labeled black triangles mark locations of PNSN seismographs operating in 1993, the star is the Scotts Mills mainshock epicenter, PHF indicates the Portland Hills Fault, MAF indicates the Mount Angel Fault, and gray triangles mark Quaternary volcanoes. Map border corresponds to box B in Figure 1.

together with focal mechanisms of the Woodburn earthquakes have led to the conclusion that the MAF is a result of both reverse motion and right-lateral strike-slip motion (Werner *et al.*, 1992).

Data and Instrumentation

The Scotts Mills earthquake sequence data set is a compilation of trace data collected by permanent short-period digital stations of the PNSN and by temporary digital stations installed by the U.S. Geological Survey (USGS). The Scotts Mills mainshock and initial 35 aftershocks were recorded only by the PNSN. Beginning about 12 h after the mainshock, investigators from the USGS installed temporary digital stations that collected data between 26 March and 15 April 1993 (Carver *et al.*, 1993). We first determined locations for a total of 148 earthquakes (Fig. 3), with 6 or more *P* arrivals and $M_D \geq 1.0$. In locating these events, we used data only from stations within 75 km epicentral distance. With the additional criteria of maximum azimuthal gap of 140°, and that travel times include both USGS and PNSN data, we selected a subset of 50 aftershocks, listed as events 2 through 51 in Table 1, for more detailed analysis. The average numbers of *P* picks and *S* picks per event are 31.5 and 5.6, respectively, and the *S* picks come exclusively from the USGS data.

The USGS temporary station deployment comprised a total of 30 sites in the Scotts Mills area (see Carver *et al.*, 1993), mostly within 10 km of the mainshock epicenter (Fig. 3). The two PNSN stations nearest the mainshock epicenter, SSO and VG2, were located at epicentral distances of 22 and 28 km, respectively (Fig. 2). Table 2 lists the pertinent station characteristics, and Table 3 summarizes the characteristics of the recording instruments. All USGS seismographs in the Scotts Mills area sampled data at 200 samples per second, and triggered recording durations were typically about 30 sec.

Data recorded on the temporary seismographs were formatted and archived by the Denver and Menlo Park offices of the USGS. We combined these data with PNSN data. Uncertainties in aftershock locations, initially determined using only PNSN data, were reduced by as much as a factor of 10 after the merging of the additional temporary station data. Preliminary analysis using only the PNSN data was inconclusive; thus, the results presented here depend critically on the combination of data.

Analysis

Methods

As our starting velocity model for aftershock locations, we chose the 1D layered model routinely used for the Puget Sound basin, model PS (Crosson, 1976), because the Willamette Valley is geologically similar to the Puget Sound basin. To determine an average V_P/V_S for the Scotts Mills area, we chose four moderate-sized events (numbers 8, 14, 15, and 47 in Table 1) and plotted the Wadati diagram, where *S* arrival times were determined only from horizontal-component data. This analysis could not be performed with larger aftershocks because the *S* arrival onsets were obscured by *P* codas. From this analysis, we found $V_P/V_S = 1.78$ (Poisson's ratio of 0.27). By contrast, the Puget Sound basin has a V_P/V_S of 1.73, where *S* arrivals are estimated primarily from vertical-component data. To construct our final velocity model, SM9, given in Table 4, we used the *P* velocities of the PS model and decreased *S* velocities so that $V_P/V_S = 1.78$.

To illustrate the difficulty in making *S* picks on vertical-component seismograms, we compare horizontal and vertical components from USGS station YOD with a seismogram from PNSN station SSO in Figure 4. Because of this difficulty, our analysis used only *S* arrival times picked on horizontal components of the temporary USGS stations. We note that our mainshock depth determination of 15.1 km, based only on PNSN *P* arrival times, is greater than the 12- to 13-km depth found by waveform inversion of regional broadband trace data (Nábelek and Xia, 1995). However, the lack of close-in stations that provide depth constraint makes the mainshock depth subject to greater uncertainty than the aftershocks.

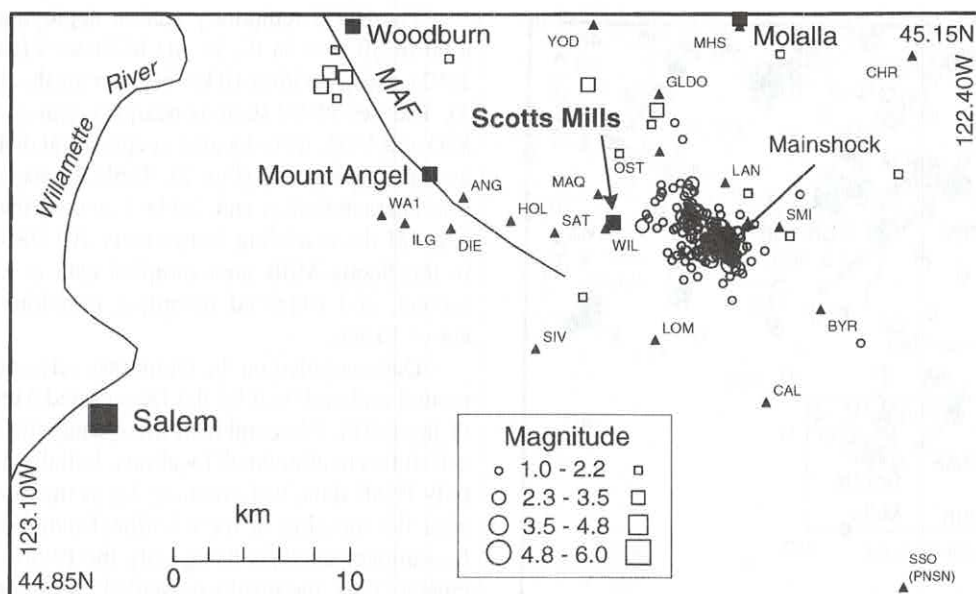Station travel-time corrections for USGS and PNSN sta-

Figure 3.   Map of Scotts Mills area. Triangles mark the locations of the USGS temporary seismograph stations and nearest PNSN station, SSO. Circles mark 148 epicenters of the Scotts Mills earthquake sequence through the end of July 1994, as determined in this study, and squares mark background seismicity for 1989 through February 1993, as listed in the PNSN catalog. MAF designates the Mount Angel Fault as inferred by Werner *et al.* (1992). Map boundary corresponds to box A in Figure 1.

tions were determined using a master event method. We chose two candidate events (14 and 15, in Table 1), based on a minimum of 15 *P* arrivals at temporary stations, and an azimuthal gap of less than 35°. We then investigated the hypocentral numerical variability of these two aftershocks in relationship to the other aftershocks, by applying the following jackknife-type analysis to each event.

For each earthquake, we started with a complete set of arrival times, deleted a random selection of 10% of the arrival times, and estimated the hypocenter using the starting velocity model PS. This process was repeated, generating 50 location estimates for each event. To quantify the spatial distributions of estimated locations, we formed, for each aftershock, a standard second moment, or "inertia," tensor (e.g., Arfken, 1985, pp. 217–218), assigning nondimensional unit "mass" to each estimated location. For each tensor, we found I_0, the root mean square (RMS) of the three principal moments (inertia tensor eigenvalues). For events 2 through 51 in Table 1, the I_0 values spanned two decades, ranging from about 0.01 km^2 to about 1 km^2. In particular, events 14 and 15 had I_0 values of 0.060 and 0.067 km^2, respectively. Approximately 70% of the events had larger values. Aftershocks with the smallest I_0 were interpreted as having the most stable locations.

Events 14 and 15 were then tested individually as master events. Station corrections were determined from each event, and the aftershocks were relocated. We found that RMS travel-time residuals, averaged over all aftershocks, equaled 0.16 sec for event 14 and 0.19 sec for event 15. Both values

are smaller than the 0.24-sec average RMS residual for the PS model without station corrections and the 0.23-sec average RMS residual for model SM9 without station corrections. Finally, we selected event 14 as the best master event, and its travel-time residuals were used as station corrections for all aftershock locations.

Aftershock Locations

The mainshock and all aftershocks were relocated using the SM9 velocity model and the master event station corrections. Most aftershock depths fall in the depth range of 8 to 15 km. Although there is somewhat more scatter in depth for aftershocks prior to installation of the temporary stations, there does not appear to be a systematic bias in depth for aftershocks located only with data from PNSN stations. In performing waveform analysis of the 1990 Woodburn earthquakes, Werner *et al.* (1992) found focal depths in the 15- to 20-km range, while the PNSN catalog depths for the same earthquakes were around 30 km. Applying our location scheme to those same events gave focal depths around 17 km. From this, we infer that our model and station corrections provide quality locations for earthquakes in the Scotts Mills region, even when only PNSN data are available.

Figure 5 shows relocated epicenters of the subset of 50 aftershocks that have both USGS and PNSN data; the final locations are also listed in Table 1. The average of the formal standard errors in the vertical direction is 0.26 km. Figure 6 shows orthogonal cross sections of hypocenters of this subset of aftershocks, with projection planes striking north-

Table 1
Earthquake Locations*

Event	Date (Yr Mo Day)	Time (hr:min)	Latitude (°N)	Longitude (°W)	Depth (km)	M_D	Gap (°)	RMS residual (sec)
1	93 03 25	13:34	45.033	122.586	15.1	5.6	66	0.27
2	93 03 26	05:18	45.033	122.597	12.6	2.9	67	0.24
3	93 03 26	07:35	45.023	122.583	11.3	1.8	66	0.20
4	93 03 26	07:59	45.032	122.599	12.2	2.9	67	0.18
5	93 03 26	10:22	45.027	122.579	11.4	1.7	84	0.21
6	93 03 26	12:55	45.020	122.611	11.7	2.0	68	0.23
7	93 03 26	16:54	45.028	122.605	11.2	3.1	67	0.27
8	93 03 26	17:39	45.047	122.611	13.8	3.2	67	0.21
9	93 03 26	18:43	45.059	122.613	10.7	2.8	67	0.14
10	93 03 26	19:56	45.050	122.591	14.0	1.5	135	0.28
11	93 03 27	05:40	45.030	122.576	12.7	2.6	34	0.21
12	93 03 27	06:46	45.058	122.632	9.6	2.1	47	0.19
13	93 03 27	13:41	45.043	122.632	11.4	1.2	68	0.16
14	93 03 27	14:38	45.041	122.589	13.9	2.9	29	0.00
15	93 03 27	22:24	45.030	122.592	12.4	2.5	32	0.13
16	93 03 27	22:31	45.028	122.628	10.3	1.1	123	0.12
17	93 03 27	23:34	45.028	122.608	11.3	1.7	39	0.15
18	93 03 28	05:22	45.028	122.594	11.6	2.1	32	0.19
19	93 03 28	07:43	45.029	122.596	11.6	1.8	73	0.22
20	93 03 28	08:20	45.040	122.606	12.7	1.5	64	0.14
21	93 03 28	08:50	45.036	122.601	13.6	1.7	53	0.13
22	93 03 28	09:03	45.035	122.600	13.5	1.6	53	0.14
23	93 03 28	15:50	45.031	122.618	11.0	1.7	68	0.16
24	93 03 28	23:26	45.030	122.604	11.7	1.4	62	0.12
25	93 03 29	00:16	45.043	122.594	13.5	2.0	32	0.12
26	93 03 29	02:19	45.030	122.589	11.7	2.0	55	0.23
27	93 03 29	10:39	45.029	122.615	11.1	1.5	65	0.21
28	93 03 29	22:47	45.057	122.616	10.7	1.9	47	0.13
29	93 03 30	05:49	45.040	122.624	12.5	1.1	111	0.02
30	93 03 30	07:43	45.023	122.583	11.8	1.7	99	0.17
31	93 03 30	09:18	45.043	122.609	13.4	1.3	120	0.03
32	93 03 30	11:36	45.040	122.636	11.8	1.1	109	0.05
33	93 03 30	11:41	45.041	122.606	13.3	1.7	52	0.15
34	93 03 30	15:29	45.030	122.596	13.2	1.1	126	0.12
35	93 03 30	16:56	45.059	122.609	11.0	1.6	68	0.21
36	93 03 30	17:30	45.016	122.607	9.8	1.4	129	0.29
37	93 03 31	08:35	45.042	122.596	13.9	1.5	77	0.11
38	93 03 31	13:16	45.024	122.616	10.6	1.4	136	0.08
39	93 03 31	19:28	45.042	122.593	13.6	1.8	96	0.26
40	93 03 31	23:43	45.042	122.611	12.8	1.0	69	0.06
41	93 04 01	04:13	45.023	122.582	11.2	1.3	112	0.04
42	93 04 01	04:35	45.037	122.587	13.0	1.2	130	0.05
43	93 04 01	05:10	45.023	122.580	11.4	1.1	66	0.04
44	93 04 01	09:37	45.025	122.583	11.2	1.1	62	0.03
45	93 04 01	09:39	45.038	122.590	12.9	1.2	79	0.07
46	93 04 05	06:38	45.019	122.579	12.0	2.2	132	0.18
47	93 04 06	09:47	45.042	122.646	11.6	2.6	79	0.16
48	93 04 07	04:32	45.043	122.615	14.3	2.5	67	0.26
49	93 04 07	20:51	45.045	122.642	12.6	2.2	78	0.25
50	93 04 08	06:24	45.038	122.618	13.2	2.3	106	0.32
51	93 04 15	06:44	45.017	122.575	13.4	2.2	82	0.33
a	93 03 25	14:20	45.027	122.586	12.5	3.1	66	0.27
b	93 03 25	15:35	45.028	122.589	13.4	3.2	66	0.28
c	93 06 08	00:01	45.022	122.583	13.9	3.9	66	0.33
d	93 04 30	23:01	45.042	122.596	14.9	2.5	66	0.10

*Event 1 is the mainshock; events 2 through 51 are the subset of aftershocks that combine USGS and PNSN data; and events *a* through *d* are additional aftershocks with focal mechanisms shown in Figure 7, but located only with PNSN data.

Table 2
Locations of USGS Temporary Stations and Two Closest PNSN Stations

Station Name	Recorder Type	North Latitude (deg. min. sec.)	West Longitude (deg. min. sec.)	Elevation (km)	Date Installed*	Date Removed
ANG	GEOS	45 03 22.14	122 46 29.70	0.128	3/30	4/14
BC1	Reftek	45 01 44.10	122 37 04.80	0.192	3/27	4/01
BYR	DR-200	44 59 56.40	122 31 07.32	0.660	3/28	4/01
BYR	GEOS	44 59 56.40	122 31 07.32	0.660	4/01	4/15
CAL	DR-200	44 57 03.80	122 33 29.20	0.615	3/26	4/01
CAL	GEOS	44 57 03.80	122 33 29.20	0.615	4/01	4/14
CHR	GEOS	45 07 42.20	122 27 06.90	0.349	3/27	3/30
DIE	DR-200	45 02 25.08	122 47 01.70	0.064	3/27	4/01
GLDO	GEOS	45 06 33.00	122 38 02.00	0.091	3/26	3/29
HA1	Reftek	45 30 00.00	122 39 00.00	0.018	3/23	3/28
HOL	DR-200	45 02 39.12	122 44 26.40	0.092	3/27	4/01
ILG	DR-200	45 02 35.40	122 49 00.50	0.052	3/27	3/28
LAN	DR-200	45 03 48.80	122 35 12.48	0.207	3/26	4/01
LOM	DR-200	44 59 00.60	122 38 14.40	0.277	3/26	4/01
MAQ	GEOS	45 03 27.60	122 40 41.40	0.116	3/27	3/30
MHS	GEOS	45 08 37.80	122 34 32.90	0.117	3/27	3/30
OST	DR-200	45 04 46.80	122 38 01.10	0.159	3/26	4/01
OST	GEOS	45 04 46.80	122 38 01.10	0.159	3/31	4/11
SAT	DR-200	45 02 17.10	122 42 33.50	0.181	3/27	4/01
SIV	GEOS	44 58 44.40	122 43 22.75	0.308	3/27	4/14
SMI	DR-200	45 02 27.30	122 32 53.52	0.415	3/26	4/01
SMI	GEOS	45 02 27.30	122 32 53.52	0.415	3/31	4/14
SSO	PNSN	44 51 21.60	122 27 37.80	1.242	9/91	—
VG2	PNSN	45 09 20.00	122 16 15.00	0.823	9/85	—
WA1	Reftek	45 02 49.58	122 50 00.53	0.056	3/27	4/01
WB1	Reftek	45 02 49.62	122 50 09.46	0.056	3/27	4/01
WC1	Reftek	45 02 43.99	122 50 04.98	0.055	3/27	4/01
WIL	DR-200	45 02 24.60	122 40 23.10	0.216	3/27	3/29
YOD	GEOS	45 08 40.50	122 40 51.75	0.067	3/27	3/30

*Installation and removal dates are given in month/day of 1993, except the PNSN stations, where the installation dates are listed in month/year.

Table 3
Summary of Digital Seismograph Parameters

Recorder Type	Deployment Group	Number of Channels*	Sensor*	Sensor Natural Frequency, f_0 (Hz)	Sample Rate (Samples/sec)	Dynamic Range (bits)
GEOS	Menlo Park	3/3	L-22/FBA	2.0/80.0*	200.0	16
DR-200	Denver	3/0	S-6000†	2.1/1.7‡	200.0	16
Reftek§	Golden	3/3	L-22/FBA	2.0/50.0*	200.0	16
PNSN	PNSN	1/0	L-4C or S-13	1.0	101.016	14

*Velocity/acceleration.
†Except station BYR with an L-22 sensor.
‡Vertical/horizontal components, except station BYR, which had $f_0 = 2.0$ for all components.
§Stations BC1 and HA1 had six acceleration channels with $f_0 = 50.0$ Hz, and station HA1 had a sample rate of 100 samples/sec.

northeast and east-southeast. The cross sections show a steeply dipping planar structure with strike $290 \pm 10°$ and dipping $60 \pm 5°$ to the north-northeast, determined by visual inspection. We refer to this planar structure as the Scotts Mills Seismic Zone (SMZ) and interpret it as a subsurface oblique reverse fault. Hypocenters of four events in Figure 6 are well removed from the SMZ and may lie on an auxiliary fault or faults. The observed planar structure does not appear to be an artifact of station geometry or location method. It has persisted through several relocation schemes with several different velocity models as well as various station corrections (including zero station corrections). However, to further test for the possibility that hypocenter uncertainty may contribute to the apparent alignment, we repeated the previously described jackknife analysis on the relocated events (2 through 51 in Table 1) using our final model and

Table 4
Model SM9

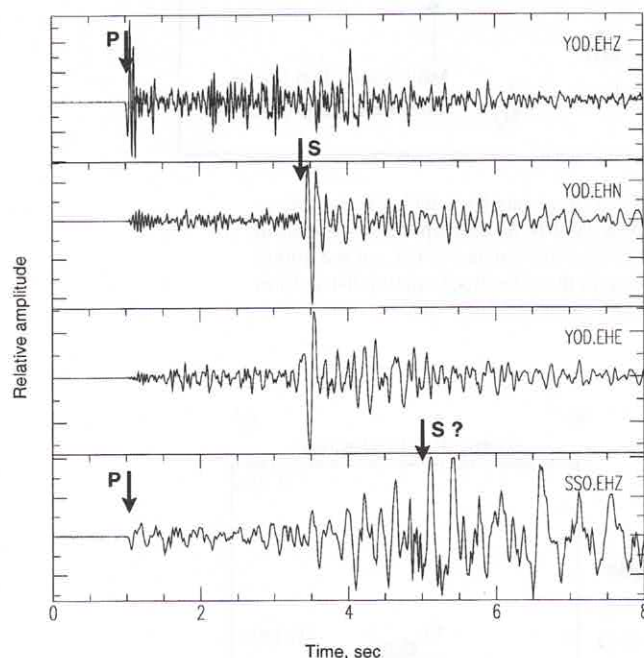| Depth (km)	V_P (km/sec)	V_S (km/sec)
0.0	5.36	3.01
10.0	6.61	3.71
16.0	6.70	3.76
22.0	6.91	3.88
32.0	7.11	3.99
35.0	7.16	4.02
38.0	6.87	3.86
41.0	7.75	4.35

Figure 4. Unfiltered velocity seismograms for event 12. The top three traces are the high gain vertical, north, and east components, respectively, of USGS station YOD (10.4 km epicentral distance), and the bottom trace is PNSN station SSO (26.2 km epicentral distance). Traces are aligned on the *P* arrival.

station corrections. The results did not show preferential location dispersion alignment along the SMZ. Also, using standard-error ellipse analysis, we found that the major axes of the error ellipses were not preferentially aligned in the plane of the aftershock distribution.

Focal Mechanisms

Using *P*-wave first motions and the layered velocity model SM9, we fit double-couple focal mechanism solutions to the mainshock and 10 aftershocks. Mechanisms for six of the aftershocks utilize both USGS and PNSN data; the mainshock and four aftershocks (events *a* through *d* in Table 1) utilize PNSN data only. Lower-hemisphere equal-angle projections are plotted in Figure 7.

The focal mechanism solution from *P*-wave first motions agrees well with the solution determined by waveform inversion of regional broadband data (Nábelek and Xia, 1995) and waveform inversion of teleseismic data (Nábelek and Xia, 1995; Dewey *et al.*, 1994). The northwest-trending nodal plane for the mainshock solution, strike 294° and dip of 58° to the north-northeast, has a geometry similar to the planar structure of the aftershock distribution. We infer that this northwest-striking nodal plane is the slip plane of Scotts Mills mainshock. With a rake of 138°, the motion on this slip plane is oblique thrust, with approximately a 1:1 ratio of strike slip to reverse motion.

Focal mechanisms for the aftershocks (Fig. 7) exhibit significant variability, ranging from nearly pure strike slip to nearly pure reverse motion. The largest aftershocks in the sequence (events 8 and *a* through *d*, in Table 1) have solutions generally similar to the mainshock (right-lateral strike slip with a smaller component of reverse motion). The largest aftershock of the entire Scotts Mills sequence (event *c*, $M_D = 3.9$), occurring on 8 June 1993, has a solution quite similar to the first located aftershock (event *a*, $M_D = 3.1$) that occurred 1 hr after the mainshock. Events *a* and *c* both have solutions with northwest-trending nodal planes, striking 336° and 333°, respectively, and dipping 63° and 44°, respectively, to the northeast.

While the focal mechanisms vary, the *P* axes and inferred directions of maximum stress are quite consistent. A combined *P* and *T* axis distribution, shown in the inset of Figure 7, shows that *P* axes tend to horizontal and clustered about a north–south direction. This is in excellent agreement with an approximate N10°E direction of maximum horizontal compressive stress as determined by borehole breakouts in both northwest Oregon (Werner *et al.*, 1991), and Puget Sound, Washington (Magee and Zoback, 1992), but is rotated substantially from the N50°E direction of convergence between the Juan de Fuca and North America plates (e.g., Riddihough, 1984). The north–south orientation of *P* axes is also consistent with focal mechanism studies of crustal earthquakes in western Washington (e.g., Ma *et al.*, 1991; Crosson, 1972, 1983), eastern Washington (Malone *et al.*, 1975), and Vancouver Island (Rogers, 1979). A tectonic model for the Pacific Northwest that adequately relates the oblique oceanic-continental convergence to the observed north–south regional compressive stress is a subject of continuing research.

Frequency-Magnitude Relations

Magnitude calculations were made using the coda duration scheme of Crosson (1972), modified to use the median rather than the mean duration. Durations were measured from the *P* onset to a time where the signal level was twice the presignal noise level. Durations were chosen only on USGS stations HOL, LAN, OST, and WIL (Table 2), and PNSN stations BPO, FBO, MTM, TKO, VBE, and VLM (Ludwin *et al.*, 1994), all within 75 km epicentral distance. Mainshock durations could not be measured from digital data because the PNSN data were truncated. Instead, durations were de-
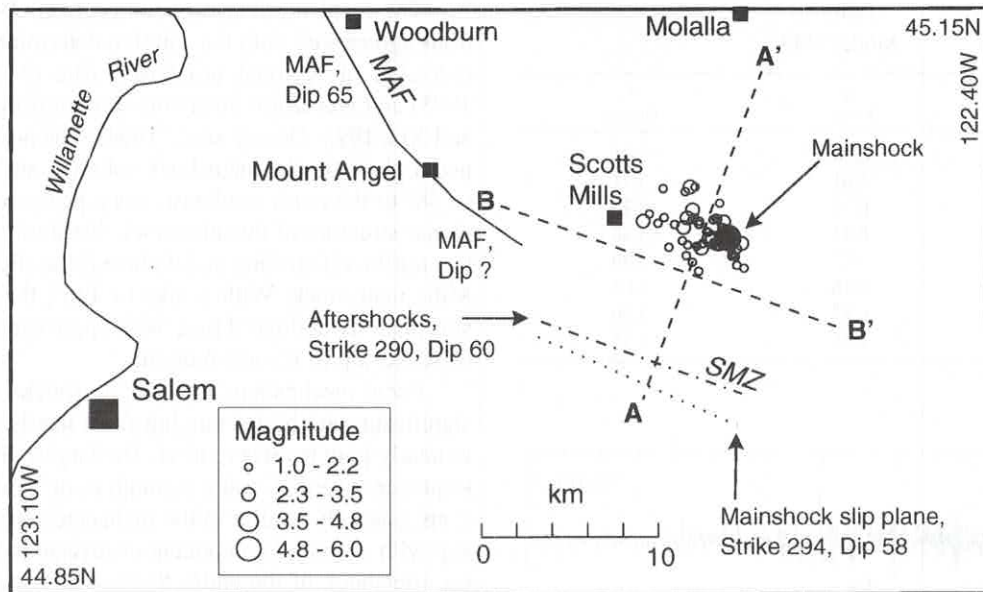
Figure 5.   Circles mark epicenters of a subset of 50 events for which we are able to combine USGS and PNSN data. Dashed lines A-A′ and B-B′ correspond to projection planes of the cross sections in Figure 6. Dash-dot line (designated SMZ) and the dotted line are surface projections of the planar structure in the aftershock spatial distribution and the mainshock focal mechanism preferred slip plane, respectively.
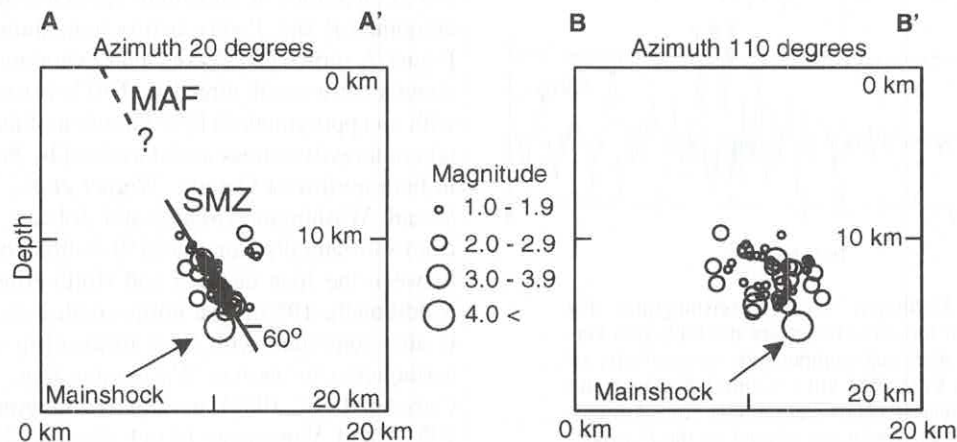
Figure 6.   Orthogonal cross sections of earthquakes shown in Figure 5. In section A-A′, we find that 46 of the 50 earthquakes appear to form a steeply dipping planar structure (SMZ). Four outlier events are located to the north (right) of the general trend. The dashed line marks the projection of the MAF. Section B-B′ shows that the mainshock occurred at the deepest part of the SMZ. Point A is located at 44.95° N, 122.65° W, and point B is located at 45.05° N, 122.75° W.

termined from analog records of four PNSN stations. The local Richter magnitude estimate for the mainshock is based on amplitudes recorded by horizontal-component digital PNSN stations (SEE and SEN) with simulated Wood-Anderson responses.

Cumulative frequency-magnitude data for the earthquake sequence through the end of 1993 (132 earthquakes)

are plotted in Figure 8. There is a linear trend in the plot for aftershocks in the range $1.7 < M_D < 3.3$ that conforms to the standard Gutenberg-Richter relation,

$$\log(N) = a - bM,$$

where N is the number of earthquakes with magnitude

Figure 7. Map of epicenters and corresponding focal mechanisms. Filled diamonds mark epicenters of events for which mechanisms were fit to USGS and PNSN data 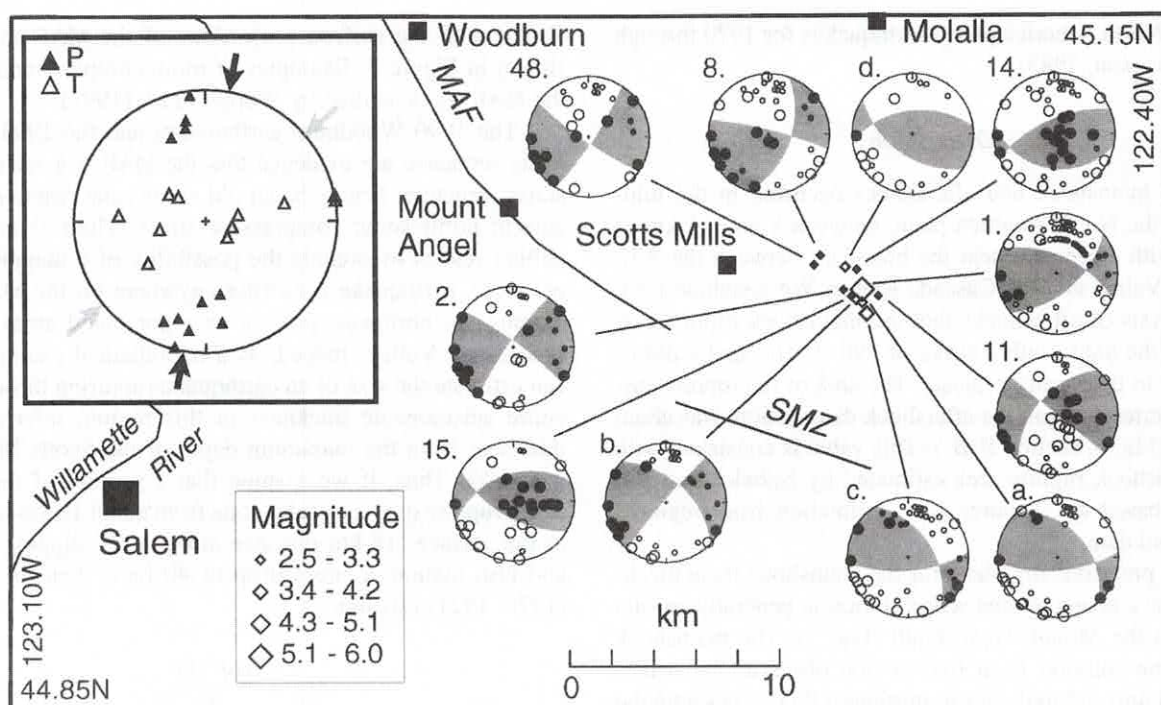while open diamonds were fit to PNSN data only. Focal mechanisms are plotted as lower-hemisphere equal-angle projections. Within each focal mechanism, filled circles represent compressional first motion, and open circles are dilatational. Larger circles correspond to rays that travel through the upper hemisphere. The inset shows the composite projection of *P* and *T* axes for all 11 focal mechanism solutions. Filled triangles are *P* axes, and hollow triangles are *T* axes. The dark arrows indicate the N10° E direction of maximum horizontal compressive stress in northwest Oregon found from borehole studies (Werner *et al.*, 1991), and the gray arrows indicate the N50°E direction of convergence between the subducting Juan de Fuca plate and overriding North America plate (e.g., Riddihough, 1984).
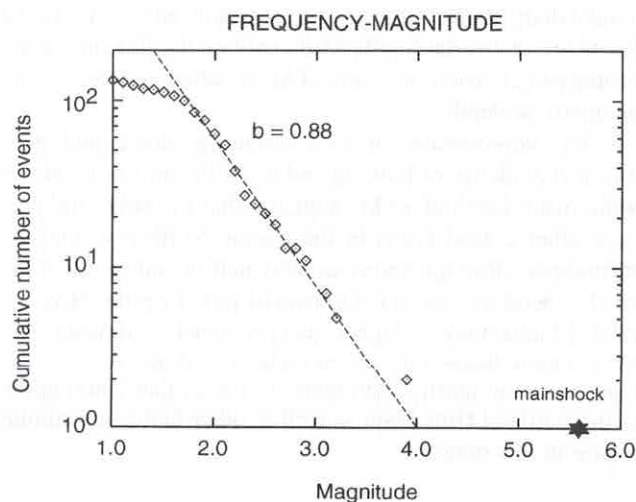
Figure 8. Magnitude-frequency plot for the Scotts Mills earthquake sequence for events from 25 March through 31 December, 1993.

greater than *M*, and *a* and *b* are constants. For $M_D < 1.7$, the departure from the linear trend is interpreted as an indication of a threshold magnitude of about 1.7 for reliable detection by the PNSN in the Scotts Mills area. The threshold magnitude of about 1.7 is also observed in similar plots with time windows that exclude the USGS data. For the Scotts Mills aftershock sequence through the end of 1993, we find $b = 0.88 \pm 0.16$, determined by the method of maximum likelihood estimation discussed in Shi and Bolt (1982), with a threshold magnitude of 1.7. The large uncertainties are the result of a relatively small total number of events (100 of magnitude 1.7 or larger). A curve with this slope is plotted as a dashed line in Figure 8.

The *b* value of 0.88 for the Scotts Mills aftershock sequence is slightly greater than *b* values for other aftershock sequences in the Pacific Northwest, such as 0.77 ± 0.05 for the Elk Lake aftershock sequence of 1981 (Grant *et al.* 1984) and 0.67 ± 0.01 for the posteruptive Mt. St. Helens sequence of 1980 (Weaver *et al.*, 1981). However, the above values are smaller than the *b* value of 1.02 for Puget Sound

crustal (North America plate) earthquakes for 1970 through 1978 (Crosson, 1983).

Discussion

The mainshock and aftershocks occurred in the mid-crust of the North America plate, between 8 and 15 km in depth, with epicenters near the boundary between the Willamette Valley and the Cascade Range. We conclude from our analysis of aftershocks that the mainshock ruptured on a plane, the SMZ, with a strike of 290 ± 10°, and a dip of 60 ± 5° to the north-northeast. The area of the rupture surface, as inferred from the aftershock distribution, was about 28 km² (Fig. 6, section B-B'). This value is consistent with the mainshock rupture area estimated by Nábelek and Xia (1995), based on a source time estimation from regional broadband data.

The preferred slip plane for the mainshock focal mechanism has a geometry and sense of motion generally consistent with the Mount Angel Fault (Fig. 7). The mainshock fault-plane solution from first-motion observations strikes 294° and dips 58° to the north-northeast; this agrees with the aftershock distribution. In comparison, the southeast portion of the MAF has a mapped strike of 305° (Werner et al., 1992). Although the dip of the southeast section of the MAF is poorly constrained, the northwest part of the MAF has a dip of 65° to the northeast, based on a single seismic reflection line 2 km southeast of Woodburn (Werner et al., 1992). The sense of motion of the Scotts Mills mainshock and several aftershocks, a combination of reverse and right-lateral strike-slip motion, is consistent with interpretations of post-Miocene displacement on the southeast section of the MAF. The strike of the MAF apparently changes as it enters the Willamette Valley, as shown in Figure 7. The northwest portion of the MAF, near Woodburn, has a mapped strike of 330°. In addition, Werner et al. (1992) determined a composite focal mechanism for the 1990 Woodburn earthquakes and for those earthquakes inferred right-lateral motion on a plane striking 350 ± 10°. This value is significantly different from the trend of the southeast portion of the MAF and the strike of the Scotts Mills mainshock slip plane.

We propose two alternative structural models for the relationship between the MAF and the SMZ. In the first model, the "fault zone model," the MAF is a zone consisting of several discrete faults. In this model, the MAF "zone" has a length of at least 25 km, and the fault strikes range from 290°, in the Cascade foothills, to up to 350° in the Willamette Valley near Woodburn. In this model, the Scotts Mills earthquake and aftershocks occurred on one fault within the zone. We note that Werner et al. (1992) interpret the northwest portion of the MAF as consisting of several faults, based on a seismic reflection line through Woodburn. An alternative model, the "listric model," is that the MAF is a single but curved fault. The dip decreases with depth and the strike becomes more westerly toward the southeast end of the fault. In this model, the Scotts Mills earthquake occurred on the southeastern end of the MAF. Both of these models are con-

sistent with the surface projections of the MAF and SMZ shown in Figure 7. Examples of more complex models for the MAF are described by Werner et al. (1992).

The 1990 Woodburn earthquakes and the 1993 Scotts Mills sequence are evidence that the MAF is a seismically active structure. It may be an old shear zone reactivated by current north–south compressive stress. There is no compelling reason to exclude the possibility of a magnitude 6, or larger, earthquake occurring anywhere on the MAF, including the northwest portion near populated areas of the Willamette Valley. Indeed, as a hypothetical example, we can estimate the size of an earthquake rupturing through the entire seismogenic thickness in this region, inferring the thickness from the maximum depth of the Scotts Mills aftershocks. Thus, if we assume that a portion of the MAF could rupture over a circular zone from about 16 km in depth to the surface (18-km distance along a 60° dipping plane) and also assume a stress drop of 40 bars, then the Brune (1970, 1971) relation,

$$M_0 = \frac{16 r^3 \Delta\sigma}{7},$$

gives a moment estimate of 6.7×10^{25} dyne-cm, corresponding to an $M_w = 6.5$ earthquake.

Conclusion

Aftershocks of the Scotts Mills earthquake align on a plane striking 290° and dipping 60° to the north-northeast. The mainshock focal mechanism is consistent with oblique thrust on this plane, driven by north–south tectonic stress. Comparison of the rupture surface with the orientation and position of the Mount Angel Fault suggests a close connection between the Scotts Mills earthquake and the MAF. Two alternatives are (a) the Scotts Mills earthquake occurred on a subsidiary fault within a complex fault zone comprising the MAF, or (b) the Scotts Mills earthquake lies on a deep southeast extension of a curved MAF, which exhibits listric geometry at depth.

The combination of near-surface geologic and geophysical evidence of faulting and a significant earthquake at mid-crustal depth of 15 km suggests that the MAF, and perhaps other crustal faults in the Pacific Northwest, may be seismogenic through approximately half the thickness of the crust. Therefore, the seismic hazard posed by the MAF, or related faults, may be higher than previously estimated. The MAF may indicate a dominant style of faulting, activated or reactivated by north–south tectonic stress, that could apply to the Portland Hills Fault as well as other faults of a similar nature in this region.

Data Availability

The Scotts Mills digital data set (~250 Mb) is available upon request. This includes trace data and arrival time data recorded by USGS and PNSN seismographs.

Acknowledgments

References

Arfken, G. (1985). *Mathematical Methods for Physicists,* Academic Press, Inc., San Diego, California, 985 pp.

Beeson, M. H., K. R. Fecht, S. P. Reidel, and T. L. Tolan (1985). Regional correlations within the Frenchman Springs Member of the Columbia River Basalt Group: new insights into the middle Miocene tectonics of northwestern Oregon, *Oregon Geol.* **47,** 87–96 (published by the Oregon Department of Geology and Mineral Industries).

Beeson, M. H., T. L. Tolan, and J. L. Anderson (1989). The Columbia River Basalt Group in Western Oregon: geologic structures and other factors that controlled the flow emplacement patterns, in *Volcanism and Tectonism in the Columbia River Flood-Basalt Province,* S. P. Reidel and P. R. Hooper (Editors), *Geol. Soc. Am. Spec. Pap.* **239,** 233–246.

Braunmiller, J., J. Nábelek, B. Leitner, and T. Qamar (1995). The 1993 Klamath Falls, Oregon, earthquake sequence: source mechanisms from regional data, *Geophys. Res. Lett.* **22,** 105–108.

Brune, J. N. (1970). Tectonic stress and the spectra of seismic shear waves from earthquakes, *J. Geophys. Res.* **75,** 4997–5009.

Brune, J. N. (1971). Tectonic stress and the spectra of seismic shear waves from earthquakes: corrections, *J. Geophys. Res.* **76,** 5002.

Carver, D., D. Worley, and T. Yelin (1993). Digital recordings of the March 25, 1993, Scotts Mills, Oregon earthquake, *U.S. Geol. Surv. Open-File Rept. 93-535.*

Crosson, R. S. (1972). Small earthquakes, structure, and tectonics of the Puget Sound region, *Bull. Seism. Soc. Am.* **62,** 1133–1171.

Crosson, R. S. (1976). Crustal structure modeling of earthquake data 2. Velocity structure of the Puget Sound Region, Washington, *J. Geophys. Res.* **81,** 3047–3054.

Crosson, R. S. (1983). Review of Seismicity in the Puget Sound region from 1970 through 1978, in *Proc. of Workshop XIV, Earthquake Hazards of the Puget Sound Region, Washington, U.S. Geol. Surv. Open-File Rept. 83-19,* 6–18.

Dehlinger, P., R. G. Bowen, E. F. Chiburis, and W. H. Westphal (1963). Investigations of the earthquake of November 5, 1962, north of Portland, *The Ore Bin* **25,** 53–68.

Dewey, J. W., B. G. Reagor, D. Johnson, G. L. Choy, and F. Baldwin (1994). The Scotts Mills, Oregon, earthquake of March 25, 1993: intensities, strong-motion data, and teleseismic data, *U.S. Geol. Surv. Open-File Rept. 94-163.*

Grant, W. C., C. S. Weaver, and J. E. Zollweg (1984). The 14 February 1981 Elk Lake, Washington, earthquake sequence, *Bull. Seism. Soc. Am.* **74,** 1289–1309.

Hampton, E. R. (1972). Geology and ground water of the Molalla-Salem slope area, northern Willamette Valley, Oregon, *U.S. Geol. Survey Water Supply Pap. 1997.*

Ludwin, R. S., A. I. Qamar, S. D. Malone, C. Jonientz-Trisler, R. S. Crosson, R. Benson, and S. C. Moran (1994). Earthquake Hypocenters in Washington and Northern Oregon, 1987–1989, and Operation of the Washington Regional Seismograph Network, *Washington Division of Geology and Earth Resources Information Circular 89,* 40 pp. (published by the Washington State Department of Natural Resources).

Ludwin, R. S., C. S. Weaver, and R. S. Crosson (1991). Seismicity of Washington and Oregon, in *Neotectonics of North America, Decade Map Volume 1,* D. B. Slemmons, E. R. Engdahl, M. D. Zoback, and D. D. Blackwell (Editors), 77–97.

Ma, L., R. S. Crosson, and R. S. Ludwin (1991). Focal mechanisms of western Washington earthquakes and their relationship to regional tectonic stress, *U.S. Geol. Surv. Open-File Rept. 91-441-D.*

Madin, I., G. Priest, M. Mabey, S. Malone, T. Yelin, and D. Meier (1993). March 25, 1993 Scotts Mills earthquake—western Oregon's wake-up call, *Oregon Geol.* **55,** 51–56 (published by the Oregon Department of Geology and Mineral Industries).

Magee, M. and M. L. Zoback. (1992). Wellbore breakout analysis for determining tectonic stress orientations in Washington State, *U.S. Geol. Surv. Open-File Rept. 92-715.*

Malone, S. D., G. H. Rothe, and S. W. Smith (1975). Details of earthquake swarms in the Columbia Basin, Washington, *Bull. Seism. Soc. Am.* **65,** 855–864.

Nábelek, J. and G. Xia (1995). Moment-tensor analysis using regional data: application to the 25 March, 1993, Scotts Mills, Oregon, Earthquake, *Geophys. Res. Lett.* **22,** 13–16.

Riddihough, R. (1984). Recent movements of the Juan de Fuca Plate System, *J. Geophys. Res.* **89,** 6980–6994.

Rogers, G. C. (1979). Earthquake fault plane solutions near Vancouver Island, *Can. J. Earth Sci.* **16,** 523–531.

Shi, Y. and B. A. Bolt (1982). The standard error of the magnitude-frequency *b*-value, *Bull. Seism. Soc. Am.* **72,** 1677–1687.

Thenhaus, P. C. (1978). A study of the October 12, 1877 Oregon earthquakes, *U.S. Geol. Surv. Open-File Rept. 78-234.*

Weaver, C. S., W. C. Grant, S. D. Malone, and E. T. Endo (1981). Post-May 18 seismicity: volcanic and tectonic implications, *U.S. Geol. Surv. Profess. Pap. 1250,* 109–121.

Werner, K. S., E. P. Graven, T. A. Berkman, and M. J. Parker (1991). Direction of maximum horizontal compression in western Oregon determined by borehole breakouts, *Tectonics* **10,** 948–958.

Werner, K., J. Nábelek, R. Yeats, and S. Malone (1992). The Mt. Angel Fault: implications of seismic-reflection data and the Woodburn, Oregon, earthquake sequence of August, 1990, *Oregon Geol.* **54,** 112–117 (published by the Oregon Department of Geology and Mineral Industries).

Yelin, T. and H. Patton (1991). Seismotectonics of the Portland, Oregon, region, *Bull. Seism. Soc. Am.* **81,** 109–130.

Yelin, T. (1992). An earthquake swarm in the north Portland (Oregon) Hills: more speculations on the seismotectonics of the Portland Basin (abstracts with programs), *Geol. Soc. Am.* **24,** 92.

Zollweg, J. E. and R. S. Crosson (1981). The Goat Rocks Wilderness, Washington earthquake of 28 May 1981 (abstract), *EOS* **62,** 966.

University of Washington
Geophysics
Box 351650
Seattle, Washington 98195-1650
(G.C.T., R.S.C.)

U.S. Geological Survey
Box 25046
Federal Center
Denver, Colorado 80225-0046
(D.L.C.)

U.S. Geological Survey
University of Washington
Geophysics
Box 351650
Seattle, Washington 98195-1650
(T.S.Y.)

Source Scaling and Moment Estimation for the Pacific Northwest Seismograph Network Using S-Coda Amplitudes

by Shawn R. Dewberry and Robert S. Crosson

Abstract Earthquake coda waves can be used for investigating both source and medium parameters. In this investigation, we introduce a method for estimating the scalar seismic moment of local earthquakes using S-coda amplitudes recorded by regional network stations. Assuming a single-scattering coda model, more than 8000 coda amplitude measurements from 78 local western Washington earthquakes (with coda-duration magnitudes from 2.4 to 5.0) are used to estimate source spectra in the narrow frequency band 2 to 12 Hz. Using a transmission model based on previous studies, we find that our source modeling best supports an omega-square, constant stress drop, far-field scaling model. An average stress drop of 32 bars is inferred for the earthquakes studied. To calibrate the moment estimation procedure, a reference event with known moment and corner frequency is required. Using a suitable reference event, we estimate moments for the remaining 77 events in the data set. The moment values range from 5.1×10^{19} to 4.4×10^{23} dyne-cm.

Introduction

Magnitudes of small local earthquakes have been routinely estimated using total coda duration for many local networks since the early 1970s (e.g., Crosson, 1972; Lee et al., 1972; Real and Teng, 1973; Herrmann, 1975; Bakun and Lindh, 1977; Chaplin et al., 1980). However, coda duration is not only difficult to estimate consistently but is also sensitive to noise, local structure, and instrument characteristics. An alternative is to consider direct phase amplitudes. However, amplitudes are often difficult to measure on the low-dynamic-range instruments found in many local and regional networks where even moderate-sized earthquakes frequently result in extensive signal clipping of the direct phase arrivals. In contrast, coda amplitudes can almost always be measured accurately after the clipped portion of the record. Additionally, coda amplitude measurements do not suffer the same degree of uncertainty as duration measurements. These features make coda amplitude measurements an attractive alternative for estimating source moment/magnitude. A goal of this study is to develop a method for estimating scalar seismic moments for small local earthquakes within the Pacific Northwest Seismograph Network (PNSN) using coda amplitude measurements.

The use of coda amplitudes for source size estimation is not new; a robust method for magnitude estimation from coda amplitude was considered by Johnson (1979) for the CEDAR system in southern California. Suteau and Whitcomb (1979) used the linear relationship between the logarithm of seismic moment, M_0, and local magnitude, M_L, to develop a functional relationship between magnitude and

both coda amplitude and duration for shallow southern California earthquakes. Also, Biswas and Aki (1984) related the coda amplitude decay with lapse time (time measured from the event origin) to known moment for two Alaskan earthquakes. Using this amplitude-moment relation, they assigned moment values to a group of smaller events. Like Biswas and Aki, we seek to estimate moment directly from coda amplitude (rather than determining a magnitude-coda amplitude relation which is then applied to an empirical moment-magnitude relation for moment estimation). Since seismic moment is the most fundamental parameter used to convey source size, moment determination directly from coda amplitudes using a robust method should prove extremely valuable in practical application.

Our method applies the single-scattering coda model of Aki and Chouet (1975) to amplitude measurements (at a given frequency and lapse time) from many sources recorded by multiple short-period stations. Source factors are common to all instruments but vary from event to event. On the other hand, site responses are common to all events but vary from station to station. We exploit the redundancy provided by a large number of measurements to construct a least-squares inversion for the estimation of source factors and site responses.

Using source factor estimates at several frequencies, we construct a portion of the source spectra for earthquakes with a range of sizes. These narrow-band source spectral estimates are then used in a spectral ratio method (e.g., Chael, 1987; Chael and Kromer, 1988; Boore and Atkinson, 1989;

Chun *et al.*, 1989; Bungum and Alsaker, 1991) to investigate and constrain the regional far-field source scaling. Unlike the previously mentioned spectral ratio studies, our study is not limited to the analysis of mainshock/aftershock sequences using direct phases. Instead, we use coda waves, which are independent of source-receiver distance and azimuth (Aki and Chouet, 1975; Rautian and Khalturin, 1978). The use of coda waves allows for events selected to be nearly uniform in their spatial distribution. Using the scaling model best constrained by the data with at least one event of known corner frequency, f_0, and moment, M_0, source factor estimates are then related directly to seismic moments through the spectral ratio.

An important additional result of this study is internally consistent network calibration using site responses generated from the coda data. With known site responses, moment estimation becomes a forward problem. Coda amplitude measurements taken from the seismogram recorded at any calibrated site can be translated in near real time to a moment estimate. As a time-domain procedure, this method of moment estimation lends itself well to automated network processing and should provide better estimates of source size compared to present methods using coda duration for the PNSN.

Modeling of Local Earthquake Coda Waves

Aki (1969) suggested the origin of local earthquake coda waves as the superposition of backscattered energy generated by weak scattering of primary waves from randomly distributed heterogeneities. Observations of similarly shaped coda amplitude decay envelopes for earthquakes of different magnitudes showed coda waves to be insensitive to direct wave source-receiver path and epicentral distance (Aki and Chouet, 1975; Rautian and Khalturin, 1978), supporting the backscattering model. The coda amplitude at a given frequency and lapse time can be described as the product of the coda source spectrum, $S(f)$, and the response of the medium to the source. For the single-backscattering model of Aki and Chouet (1975), the coda amplitude expression takes the simple form

$$A(f, t) = S(f)t^{-v} \exp\left(\frac{-\pi f t}{Q}\right), \tag{1}$$

where f is frequency, t is lapse time, and Q describes the effective coda attenuation. For body-wave scattering, $v = 1.0$, while for surface-wave scattering $v = 0.5$. A limitation of the single-scattering model occurs at long lapse times where multiple scattering becomes increasingly important due to secondary wave generation as the sampled scattering volume becomes large (Gao *et al.*, 1983a). Coda modeling by Gao *et al.* (1983a, b) expanded the single-scattering model to include multiple scattering. More recent work by Frankel and Wennerberg (1987), Wu (1985), and Wu and Aki (1988) applies energy flux and radiative transfer theory

to coda modeling. Despite the oversimplifications of the single-scattering model, it gives results that generally agree well with observations. For a comprehensive review of coda waves, see Herraiz and Espinoza (1987).

Coda Q

Attenuation is important in coda modeling and is parameterized by the seismic quality factor, Q. One method of Q determination for a local region uses the S-coda amplitudes of local earthquakes. Starting with the coda model given by equation (1) with body-wave scattering, the amplitude term is corrected for geometrical spreading, and then the expression is linearized as

$$\ln [A(f, t) \cdot t] = -bt + c, \tag{2}$$

where b and c are found by linear regression of $\ln [A(f, t) \cdot t]$ on t. The slope of the line is related to Q, as $b = \pi f/Q$. Resulting Q values may show frequency, lapse time, and/or depth dependence.

A coda Q study using this technique was performed by Havskov *et al.* (1989) for the state of Washington in the frequency range of 2 to 16 Hz. Havskov *et al.* found no significant regional dependence (excluding the Mt. St. Helens region) or depth dependence for Q. Havskov *et al.* also found Q to be frequency dependent, fitting a power-law relation of the form $Q = Q_0 f^a$, with $Q_0 = 63$ and $a = 0.97$. However, these coda Q values were limited to amplitude measurements taken at lapse times ≤ 43 sec, and application of these results at longer lapse times may not be warranted as deep scatterers may be located in rock of higher Q. Use of only the Havskov *et al.* Q model in this study could produce error because we include amplitude measurements at lapse times longer than 43 sec. Therefore, we undertook a study to determine a Q model for lapse times longer than 43 sec for comparison with the Havskov *et al.* Q model. The results and their implications are discussed in the analysis section.

Far-Field Scaling

Corner frequency (f_0) and moment (M_0) are both important parameters that affect general spectral shape and absolute scaling of a seismogram. The far-field source displacement spectrum is constant at low frequency, with the spectral height being proportional to M_0. At high frequency, the spectrum rolls off as a power of frequency. The intersection of these two regions defines f_0 (Brune, 1970). A general analytic form for the source scaling is given by

$$\Omega(\omega) = \frac{kM_0}{\left[1 + \left(\frac{\omega}{\omega_0}\right)^2\right]^{\gamma/2}}, \tag{3}$$

where $\Omega(\omega)$ is the source displacement amplitude, M_0 is seismic moment, ω is angular frequency, ω_0 is angular corner
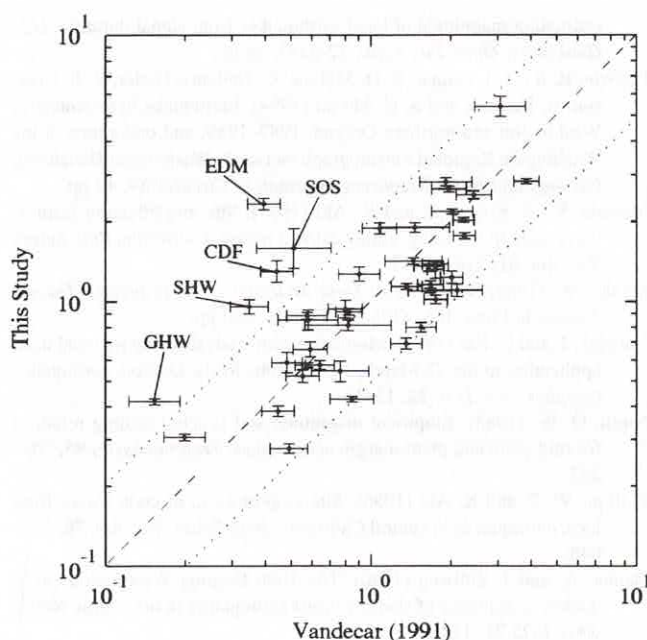
Figure 12. Log-log site response comparison of 43 sites common to this and the VanDecar (1991) study. Outliers to the data trend about a unit slope line are identified by their station names.

results is that our data set contains events sufficiently large that the source corner frequencies are generally lower than those frequencies at which the site responses strongly affect the spectra. An exhaustive investigation into the nature of site responses is beyond the scope of this study.

Implementation of the Moment Estimation Procedure

The application of our moment estimation technique to PNSN data, as part of routine earthquake analysis, is straightforward. The process involves the following general steps: (1) selecting data in the S coda of a seismogram from one or more of the calibrated stations to make an amplitude measurement while ensuring that, for each trace, the window position selected is at least twice the S lapse time and does not occur within a clipped portion of the signal. (2) Extracting the rms amplitudes from as many as five different narrow-band filtered windows in the S coda and in the presignal region, testing the signal-to-noise ratio, and discarding data with signal-to-noise <3. (3) For each acceptable measurement at a given station, generating source factors by applying site, geometrical spreading, and attenuation corrections. (4) Using the mean of all source factors over all calibrated sites for a given frequency, substitute into equation (13) to find a frequency-specific moment estimate. (5) Assigning a final moment estimate using either the mean or median of the frequency-specific estimates. This procedure can be implemented as part of an automated processing system by replacing the analyst input at step (1) with data extracted by an algorithm that selects the data window times based on direct data characteristics. Of course, a preliminary event

origin time and location are required for the application of the coda model amplitude corrections.

Conclusions

We have demonstrated that the application of the Aki and Chouet (1975) single-scattering coda model to S-coda amplitudes from many earthquakes recorded at multiple stations permits consistent source factor and site-response estimation. Seventy-seven source factor spectral ratios, taken in the frequency band 2 to 12 Hz with respect to a reference event, provide strong support for an ω-square scaling model. Moreover, absolute scaling of these source factor estimates, as determined by one reference event of known moment, suggests the ω-square, CSD scaling model as an appropriate regional scaling model. Using this scaling model, along with one earthquake of known corner frequency and moment, moment estimates are generated from the source factor estimates with values ranging from 5.1×10^{19} to 4.4×10^{23} dyne-cm for the remaining 77 regional earthquakes in the data set.

In addition, site-response estimates generated along with the source factor estimate permit network calibration. Once the network is calibrated, source factor and moment estimation using coda amplitude measurements proceeds directly from simple calculations. This method of moment estimation not only lends itself to rapid network analysis, but also should provide improved source size estimates for locally recorded earthquakes from regional network data.

References

Aki, K. (1967). Scaling law of seismic spectrum, *J. Geophys. Res.* **72,** 1217–1231.

Aki, K. (1969). Analysis of the seismic coda of local earthquakes as scattered waves, *J. Geophys. Res.* **74,** 615–631.

Aki, K. and B. Chouet (1975). Origin of coda waves: source, attenuation and scattering effects, *J. Geophys. Res.* **80,** 3322–3342.

Aki, K. and P. G. Richards (1980). *Quantitative Seismology: Theory and Methods,* Vol. 2, W. H. Freeman and Co., San Francisco, 932 pp.

Anderson, J. G. (1986). Implication of attenuation for studies of the earthquake source, in *Earthquake Source Mechanics,* S. Das, J. Boatwright, and C. H. Scholz (Editors), American Geophysical Union, Washington, D.C., 311–318.

Anderson, J. G. and S. E. Hough (1984). A model for the shape of the fourier amplitude spectrum of acceleration at high frequencies, *Bull. Seism. Soc. Am.* **74,** 1969–1993.

Bakun, W. H. and A. G. Lindh (1977). Local magnitude, seismic moments and coda durations for earthquakes near Oroville, California, *Bull. Seism. Soc. Am.* **67,** 615–629.

Biswas, N. N. and K. Aki (1984). Characteristics of coda waves: central and southcentral Alaska, *Bull. Seism. Soc. Am.* **74,** 493–507.

Boore, D. M. and G. M. Atkinson (1989). Spectral scaling of the 1985 to 1988 Nahanni, Northwest Territories, earthquakes, *Bull. Seism. Soc. Am.* **79**, 1736–1761.

Brune, J. N. (1970). Tectonic stress and the spectra of seismic shear waves from earthquakes, *J. Geophys. Res.* **75**, 4997–5009.

Brune, J. N. (1971). Correction, *J. Geophys. Res.* **76**, 5002.

Bungum, H. and A. Alsaker (1991). Source spectral scaling inversion for two earthquake sequences offshore western Norway, *Bull. Seism. Soc. Am.* **81**, 358–378.

Chael, E. P. (1987). Spectral scaling of earthquakes in the Miramichi region of New Brunswick, *Bull. Seism. Soc. Am.* **77**, 347–365.

Chael, E. P. and R. P. Kromer (1988). High-frequency spectral scaling of a main shock/aftershock sequence near the Norwegian coast, *Bull. Seism. Soc. Am.* **78**, 561–570.

Chaplin, M. P., S. R. Taylor, and M. N. Toksöz (1980). A coda-length magnitude scale for New England, *Earthquake Notes* **51**, 15–22.

Chun, K. Y., R. J. Kokoski, and G. F. West (1989). Source spectral characteristics of Miramichi earthquakes: results from 115 P-wave observations, *Bull. Seism. Soc. Am.* **79**, 15–30.

Crosson, R. S. (1972). Small earthquakes, structure, and tectonics of the Puget Sound region, *Bull. Seism. Soc. Am.* **62**, 1133–1171.

Efron, B. and R. J. Tibshirani (1993). *An Introduction to the Bootstrap*, Chapman and Hall, Inc., New York, 436 pp.

Egbert, G. D. and J. R. Booker (1986). Robust estimation of geomagnetic transfer functions, *Geophys. J. R. Astr. Soc.* **87**, 173–194.

Frankel, A. and L. Wennerberg (1987). Energy flux model of seismic coda: separation of scattering and intrinsic attenuation, *Bull. Seism. Soc. Am.* **77**, 1223–1251.

Frankel, A. and L. Wennerberg (1989). Microearthquake spectra from the Anza, California, seismic network: site response and source scaling, *Bull. Seism. Soc. Am.* **79**, 581–609.

Gao, L. S., L. C. Lee, N. N. Biswas, and K. Aki (1983a). Comparison of the effects between single and multiple scattering on coda waves for local earthquakes, *Bull. Seism. Soc. Am.* **73**, 377–389.

Gao, L. S., N. N. Biswas, L. C. Lee, and K. Aki (1983b). Effects of multiple scattering on coda waves in three-dimensional medium, *Pure Appl. Geophys.* **121**, 3–15.

Goodall, C. (1983). Examining residuals, in *Understanding Robust and Exploratory Data Analysis*, D. C. Hoaglin, F. Mosteller, and J. W. Tukey (Editors), John Wiley and Sons, New York, 211–246.

Hanks, T. C. and H. Kanamori (1979). A moment magnitude scale, *J. Geophys. Res.* **84**, 2348–2350.

Havskov, J., S. Malone, D. McClurg, and R. Crosson (1989). Coda Q for the state of Washington, *Bull. Seism. Soc. Am.* **79**, 1024–1038.

Herraiz, M. and A. F. Espinosa (1987). Coda waves: a review, *Pure Appl. Geophys.* **125**, 499–577.

Herrmann, R. B. (1975). The use of duration as a measure of seismic moment and magnitude, *Bull. Seism. Soc. Am.* **65**, 899–913.

Johnson, C. E. (1979). I. CEDAR—an approach to the computer automation of short-period local seismic networks. II. Seismotectonics of the Imperial Valley of southern California, *Ph.D. Thesis*, California Institute of Technology, Pasadena, California, 332 pp.

Koyanagi, S., K. Mayeda, and K. Aki (1992). Frequency-dependent site amplification factors using the S-wave coda for the island of Hawaii, *Bull. Seism. Soc. Am.* **82**, 1151–1185.

Lee, W. H. K., R. E. Bennett, and K. L. Meagher (1972). A method of estimating magnitude of local earthquakes from signal duration, *U.S. Geol. Surv. Open-File Rept.*, 72-0233, 28 pp.

Ludwin, R. S., A. I. Qamar, S. D. Malone, C. Jonientz-Trisler, R. S. Crosson, R. Benson, and S. C. Moran (1994). Earthquake hypocenters in Washington and northern Oregon, 1987–1989, and operations of the Washington Regional Seismograph Network, *Washington Division of Geology and Earth Resources Information Circular 89*, 40 pp.

Mayeda, K., S. Koyanagi, and K. Aki (1991). Site amplification from S-wave coda in the Long Valley caldera region, California, *Bull. Seism. Soc. Am.* **81**, 2194–2213.

Menke, W. (1984). *Geophysical Data Analysis: Discrete Inverse Theory*, Academic Press, Inc., Orlando, Florida, 260 pp.

Nabelek, J. and G. Xia (1995). Moment-tensor analysis using regional data: application to the 25 March, 1993, Scotts Mills, Oregon, earthquake, *Geophys. Res. Lett.* **22**, 13–16.

Nuttli, O. W. (1983). Empirical magnitude and spectral scaling relations for mid-plate and plate-margin earthquakes, *Tectonophysics* **93**, 207–223.

Phillips, W. S. and K. Aki (1986). Site amplification of coda waves from local earthquakes in central California, *Bull. Seism. Soc. Am.* **76**, 627–648.

Qamar, A. and J. Zollweg (1990). The 1990 Deming Washington earthquakes: a sequence of shallow thrust earthquakes in the Pacific Northwest, *EOS* **71**, 1145.

Rautian, T. G. and V. I. Khalturin (1978). The use of the coda for determination of the earthquake source spectrum, *Bull. Seism. Soc. Am.* **68**, 923–948.

Real, C. R. and T. L. Teng (1973). Local Richter magnitude and total signal duration in southern California, *Bull. Seism. Soc. Am.* **63**, 1809–1827.

Savage, J. C. (1972). Relation of corner frequency to fault dimensions, *J. Geophys. Res.* **77**, 3788–3795.

Su, F. and K. Aki (1990). Temporal and spatial variations on coda Q^{-1} associated with the north Palm Springs earthquake of July 8, 1986, *Pure Appl. Geophys.* **133**, 23–52.

Suteau, A. M. and J. H. Whitcomb (1979). A local earthquake coda magnitude and its relation to duration, moment M_0, and local Richter magnitude M_L, *Bull. Seism. Soc. Am.* **69**, 353–368.

VanDecar, J. C. (1991). Upper-mantle structure of the Cascadia subduction zone from non-linear teleseismic travel-time inversion, *Ph.D. Thesis*, University of Washington, Seattle, Washington, 165 pp.

Wahlström, R. (1993). Comparison of dynamic source parameters for earthquakes in different tectonic regions of the northern Cascadia subduction zone, *Tectonophysics* **217**, 205–215.

Wu, R. S. (1985). Multiple scattering and energy transfer of seismic waves—separation of scattering effect from intrinsic attenuation—I. Theoretical modeling, *Geophys. J. R. Astr. Soc.* **82**, 57–80.

Wu, R. S. and K. Aki (1988). Multiple scattering and energy transfer of seismic waves—separation of scattering effect from intrinsic attenuation—II. Applications of the theory to Hindu Kush region, *Pure Appl. Geophys.* **128**, 49–80.

University of Washington
Geophysics Program
Box 351650
Seattle, Washington 98195-1650
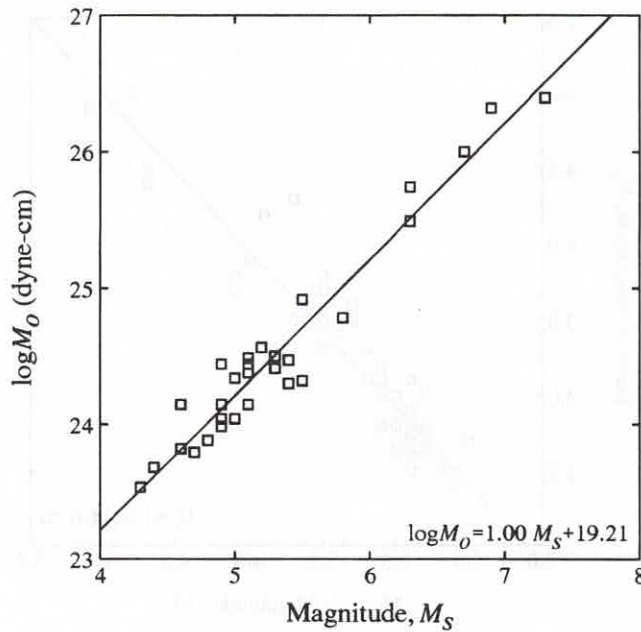
Figure 9. Moment versus surface-wave magnitude for 30 events outside Washington State used to establish a regional moment-magnitude relation. Extrapolation of the equation of the least-squares line, shown in the lower right-hand corner, to a surface-wave magnitude of 4.1 is used to estimate the moment of event 70.

Figure 10. Empirical fits of the source factor estimates in (a) to an ω-square, CSD scaling model, and in (b) to an ω-square, ISD scaling model. For a reference event (event 70) with a moment constraint of $6.30\mathrm{e}+22 \leqq M_0 \leqq 6.30\mathrm{e}+23$ dyne-cm (or $22.8 \leqq \log M_0 \leqq 23.8$), the ω-square, CSD model shows the best fit while maintaining the moment constraint.

source corner frequencies as a result of non–source related influences. Anderson and Hough (1984) and Anderson (1986) suggest that local attenuation alters the shape of the high-frequency decay of the S-wave spectra, including the region of f_0. For sites with even slight attenuation, they suggest that the observed (apparent) corner frequency is systematically smaller than the true corner frequency for events up to $M_0 < 10^{25}$ dyne-cm (**M** ~ 6). For a reasonable range of spectral decay parameters imposed on the ω-square source model by Anderson, the difference between the true and apparent corner frequencies is of the order 0.5 Hz for an **M** ~ 5 event (event 70). The discrepancy is larger for smaller events. The impact of underestimating f_0 for the reference event in our testing of scaling models is minimal, since the testing procedure included a range of f_0 values from 0.7 to 2.0 Hz. In fact, for all cases, whether the observed or slightly larger corner frequencies are used, the ω-cube models do not fit the data. The likely underestimated value of f_0 for the reference event maps into other source-parameter values expressed above, source radius and stress drop. This is not as problematic for the source radius estimate as its value is supported independently by the associated aftershock hypocenter distribution. Our stress drop estimate may be less certain because of its dependence on both M_0 and the cube of f_0. Nonetheless, uncertain values for the reference event source radius and stress drop should not detract from our

primary goal of source model constraint and moment estimation.

Moment Estimates

As a rough check on our moment estimates, we compare coda-duration magnitudes previously assigned to these events (by network analysts) to moment magnitudes generated from the Hanks and Kanamori (1979) moment-magnitude expression,

$$\log M_0 = 1.5\mathbf{M} + 16.1. \qquad (16)$$

This relation is stated by Hanks and Kanamori to be valid for $3 \leqq M_L \leqq 7$, $5 \leqq M_S \leqq 7.5$, and M_w at larger magnitudes. Moment magnitudes values generated using equation (16) for each event are given in Table 1. Figure 11 shows a plot of coda-duration magnitude versus moment magnitude with agreement between the two independently derived quantities. Linear regression of M_c on $\mathbf{M}$ results in

$$M_c = (1.04 \pm 0.04)\,\mathbf{M} - (0.20 \pm 0.14). \qquad (17)$$

The moment magnitudes derived from the moment estimates are consistent with coda-duration magnitudes for these events. This suggests the moment-magnitude relation of equation (16) may be generally valid for $2.4 \leqq M_c \leqq 5.0$ events recorded by the PNSN.

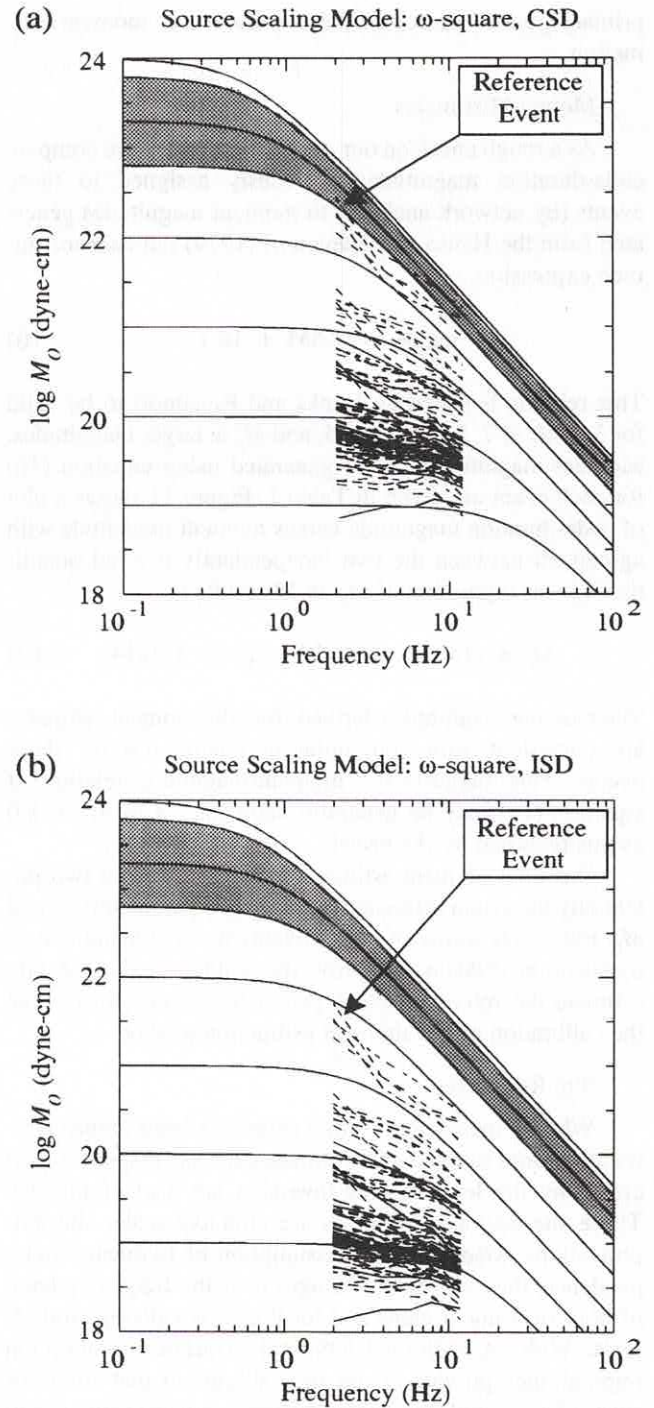Our final moment estimates are dependent on two potentially uncertain reference event source parameters, f_0 and M_0. Future recording of larger events by broadband instruments of the PNSN will improve our ability to independently estimate the reference event parameters required to refine the calibration of our moment estimation method.

Site Responses

While a major goal of this study has been moment estimation from source factor estimates, the site responses generated by the least-squares inversion are also of interest. These site-response estimates are effective scalar site amplifications. Made with the assumption of frequency independence, they represent averages over the frequency band of both instrument gains and local geological/structural effects. With an additional temporal invariance assumption implied, they provide *in situ* site calibrations that allow for source factor (and thus scalar seismic moment) estimates to be made from coda amplitudes for any local earthquakes recorded by one or more of the 47 stations included in this study. Moreover, the estimation of moments from the source spectra of calibrated stations may be easily incorporated within standard network analysis and even automated to provide efficient and rapid source size estimation.

It is interesting to compare our site-response estimates (or site amplification factors) with those from a previous study by VanDecar (1991) who generated site responses for 146 sites within the PNSN with bandlimited (0.5 to 5.0 Hz) teleseismic P-wave amplitudes using an iterative residual
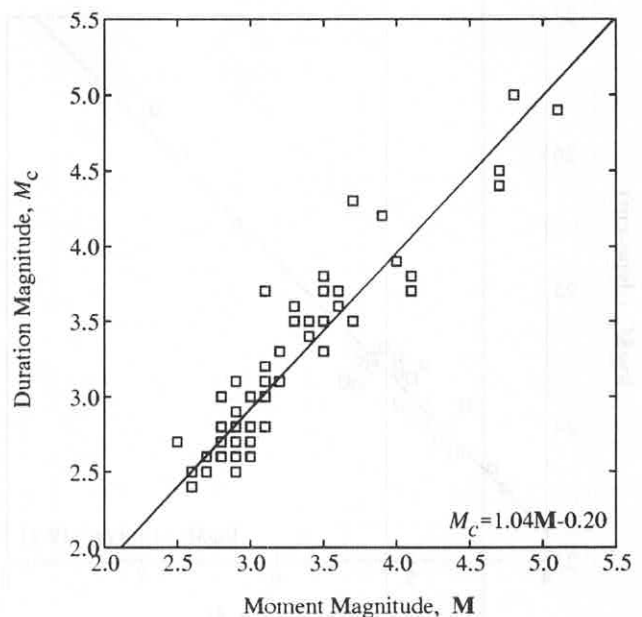
Figure 11.   Coda duration magnitude versus moment magnitude for all 78 events. Moment magnitude (**M**) values are derived using the moment estimates with the Hanks and Kanamori moment-magnitude relation (equation 16). The equation of the least-squares line is given in the lower right-hand corner.

down-weighting inversion technique. Forty-three sites common to both studies are compared. To make a meaningful comparison, the VanDecar site responses are normalized such that the geometric mean is unity. Figure 12 shows a log-log plot of the site responses; the data for all but five sites fall near a line of slope 1. Four of the five outliers (CDF, EDM, SHW, and SOS) are sites at or near Mt. St. Helens. These five outliers could result from frequency-dependent near-receiver scattering and/or attenuation. The general agreement between the site-response estimates from both studies suggests that site responses from each include the same major contributor, the station instrument gain.

In light of the work done on site amplification by recent investigators (e.g., Phillips and Aki, 1986; Frankel and Wennerberg, 1989; Mayeda *et al.*, 1991; Koyanagi *et al.*, 1992) showing systematic frequency dependence in site responses, our assumption of frequency independence must be critically examined. In addition, the observation by Frankel and Wennerberg (1989) of apparent corner frequencies that are strongly influenced by site responses needs to be further examined in light of our scaling model results. The events they analyze included microearthquakes with $M_0 < 10^{19}$ dyne-cm, with observed corner frequencies falling between 6 and 9 Hz. Their observation of moment-invariant corner frequency is contrary to the general trend of corner frequency shift observed in this study. Wahlström (1993) also found a similar increase in source corner frequency with moment for S-wave displacement spectra from earthquakes recorded near Vancouver Island. The interpretation of these
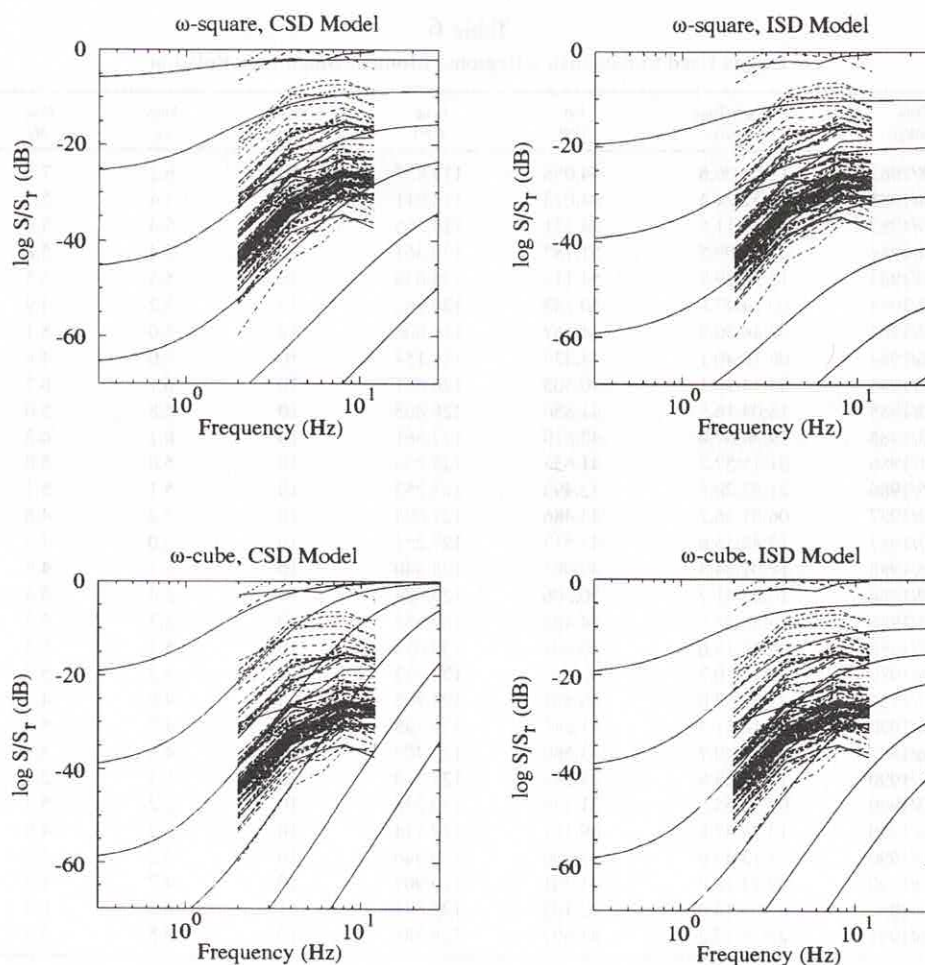
Figure 8.   Example of spectral ratio testing of four different scaling models using coda source factor spectral ratios. This example uses event 70 as the reference event with a corner frequency of 1.0 Hz.

ues of $Y = 2$, $\delta = 3$, and appropriate values of reference event $\omega_{0,r}$ and $M_{0,r}$ into equation (13), the source factor estimates for all other events can be related to moment. The solutions to equation (13) includes three analytic roots, one real and two complex. For the range in coefficient values appropriate for our data set, the complex solutions are not degenerate. The single real root is used as the solution for each of the five frequencies, and final moment estimates are assigned as the mean of the five frequency-specific values for each earthquake. The resulting mean moment values for all other events are given in Table 1; they range from 5.1×10^{19} to 4.4×10^{23} dyne-cm. It is important to note that the accuracy of these moment estimates is directly affected by the accuracy of the moment estimate for the reference event.

Discussion

Source Factor Estimates

Systematic bias of the source factor estimates is a concern. One potential source of bias could be noise at low signal levels. Those seismograms with signal-to-noise ratios at or near the cutoff may have significant noise, which could bias the measured amplitude upward. Since smaller events typically have smaller signal-to-noise ratios than the larger events, source factors and moments for small events may be overestimated.

Another potential for source factor bias could be the use of inappropriate coda Q values. Our observation of an increase in apparent coda Q with increased lapse time, along with similar observations made by other investigators (e.g., Rautian and Khalturin, 1978; Phillips and Aki, 1986; Su and Aki, 1990; Mayeda *et al.*, 1991), demonstrates the need to limit amplitude measurements to appropriate lapse-time windows. The use, for example, of coda Q determined for short lapse times (<43 sec) at longer lapse times (43 to 120 sec) overestimates the attenuation, and thus results in a larger attenuation correction to the measured amplitudes. Source factors in this case will be overestimated. Since larger events typically have larger signal-to-noise ratios at longer lapse times than smaller events, the potential for overestimating

Table 6
Events Used to Establish a Regional Moment-Magnitude Relation

Event ID	Date (m/d/yr)	Origin Time (GMT)	Lat. (°N)	Long. (°W)	Depth (km)	Mag. m_b	Mag. M_s	M_0 (dyne-cm)
1	10/28/1983	14:06:06.6	44.058	113.857	10	6.2	7.3	3.1e+26
2	10/28/1983	19:51:24.4	44.073	113.911	7	5.4	5.1	2.8e+24
3	10/29/1983	23:29:11.5	44.231	114.105	9	5.4	5.0	2.2e+24
4	06/24/1984	21:33:09.5	51.187	130.361	10	5.4	5.8	6.1e+24
5	08/30/1984	12:28:39.7	54.113	133.639	10	5.5	5.5	8.3e+24
6	08/12/1984	00:24:47.6	50.253	129.962	10	5.2	4.9	1.1e+24
7	02/22/1984	09:46:30.2	44.467	114.008	10	5.0	5.1	2.4e+24
8	08/06/1984	06:16:40.1	44.439	114.154	10	5.0	4.4	4.8e+23
9	09/10/1984	03:14:10.1	40.503	126.831	10	6.1	6.7	1.0e+26
10	07/23/1985	18:04:16.5	41.850	126.865	10	4.8	5.0	1.1e+24
11	03/13/1985	19:34:57.6	43.510	127.561	10	6.1	6.3	5.5e+25
12	02/11/1986	01:15:57.2	41.634	125.353	10	5.0	5.0	1.1e+24
13	10/05/1986	21:57:20.5	43.493	127.252	10	5.1	5.1	3.1e+24
14	06/27/1987	06:01:36.7	43.486	127.094	10	5.2	4.6	1.4e+24
15	12/07/1987	17:48:15.6	43.512	127.251	10	5.0	4.6	6.6e+23
16	05/26/1988	19:01:34.4	49.084	128.340	10	5.1	4.8	7.6e+23
17	07/19/1988	10:54:41.7	50.506	129.924	10	5.4	5.4	3.0e+23
18	10/23/1988	13:48:35.6	44.423	129.455	10	5.3	5.5	2.1e+24
19	11/27/1988	00:36:19.0	50.801	130.054	10	5.1	5.3	3.2e+24
20	05/16/1989	12:21:10.7	43.555	127.632	10	5.3	5.3	2.6e+24
21	09/21/1989	17:41:18.0	40.327	124.705	16	4.8	4.7	6.2e+23
22	01/05/1990	07:16:51.7	41.842	126.885	10	4.7	5.1	1.4e+24
23	01/16/1990	12:57:20.7	43.560	127.402	10	4.8	4.9	2.8e+24
24	01/17/1990	12:05:29.8	43.589	127.443	10	5.4	5.2	3.7e+24
25	02/03/1990	09:54:55.6	51.125	130.238	10	5.2	5.4	2.0e+24
26	02/16/1990	13:28:42.8	49.121	127.714	10	5.2	4.9	1.4e+24
27	09/20/1990	23:13:40.6	41.690	126.946	10	5.2	4.9	9.6e+23
28	09/30/1990	09:13:15.9	41.781	126.907	10	4.7	4.3	3.4e+23
29	07/13/1991	02:50:14.6	42.182	125.641	11	6.2	6.9	2.1e+26
30	08/16/1991	22:26:17.2	41.697	125.385	10	5.5	6.3	3.1e+25

the source factor estimates (and thus moment estimates), in this case, is manifest in the larger events. The incorporation of a lapse-dependent coda Q in this study decreases the likelihood of gross errors in attenuation corrections and thus source factor estimates.

Scaling Law Model

Although the spectral ratio method is useful in discriminating between various scaling-law models, the limited bandwidth of our data makes the choice of a scaling model more difficult. Intermediate or broadband data for regional and local earthquakes are needed to provide improved constraint of the scaling law. If only a single reference is used in the spectral ratio method, the results are furthermore subject to uncertainties that might exist for that event. The use of more than one reference event could improve confidence in the scale modeling results by reducing the influence of uncertainties for any single reference event.

Using the M_0 and f_0 estimates for the reference event (event 70), source dimension and stress drop are calculated for the scaling model fit by our analysis. Following Brune (1970, 1971), where

$$r = \frac{2.34\beta}{2\pi f} \qquad (14)$$

and

$$\Delta\sigma = \frac{7M_0}{16r^3}, \qquad (15)$$

we estimate a source radius of 1.4 km, assuming a β value of 3.75 km/sec and a stress drop of 32 bars. This reference event was the mainshock of a sequence of events located near Deming, Washington. Locations of aftershocks recorded by both the PNSN and a temporary seismograph array show a hypocenter distribution that is consistent with the 1.4-km source radius (Qamar and Zollweg, 1990). The 32-bar stress drop is consistent with average stress drops reported for both plate-margin earthquakes and comparably sized midplate earthquakes (Nuttli, 1983) and with the 40-bar estimate for the M_w 5.5 Scotts Mills, Oregon, earthquake (Nabelek and Xia, 1995).

The method of corner frequency determination used for the reference events is subject to error. The corner frequencies observed may well systematically underestimate the true

Table 4

(*Continued*)

ID	2 Hz $\log S_i(f)$	$(\pm \sigma)$	4 Hz $\log S_i(f)$	$(\pm \sigma)$	6 Hz $\log S_i(f)$	$(\pm \sigma)$	8 Hz $\log S_i(f)$	$(\pm \sigma)$	12 Hz $\log S_i(f)$	$(\pm \sigma)$
62	5.62	1.83e−02	5.41	1.42e−02	5.26	1.98e−02	5.09	1.70e−02	4.85	3.57e−02
63	3.45	6.70e−02	3.52	6.80e−02	3.50	3.75e−02	3.47	6.08e−02	3.38	5.91e−02
64	3.44	4.39e−02	3.55	1.18e−02	3.55	2.72e−02	3.53	3.17e−02	3.44	3.81e−02
65	4.13	6.15e−02	4.20	5.34e−02	4.16	1.53e−02	4.10	3.16e−02	3.96	7.30e−02
66	3.73	1.87e−02	3.75	4.93e−02	3.69	3.39e−02	3.66	9.46e−03	3.42	3.86e−02
67	3.16	4.10e−02	3.28	3.48e−02	3.32	2.82e−02	3.36	2.89e−02	3.24	3.80e−02
68	3.84	3.53e−02	3.81	4.53e−02	3.76	2.86e−02	3.73	3.48e−02	3.46	7.16e−02
69	3.64	2.49e−02	3.72	1.17e−02	3.75	2.20e−02	3.76	4.71e−02	3.62	4.36e−02
70	5.80	7.97e−02	5.26	6.43e−02	5.10	3.31e−02	4.91	5.36e−02	4.78	1.15e−01
71	3.53	6.49e−02	3.63	2.83e−02	3.58	5.89e−02	3.44	4.33e−02	3.17	9.57e−02
72	3.32	7.00e−02	3.38	3.36e−02	3.38	6.10e−02	3.33	5.98e−02	3.17	9.01e−02
73	4.25	6.58e−02	4.22	2.75e−02	4.14	3.19e−02	4.07	3.18e−02	3.93	2.18e−02
74	3.16	8.06e−02	3.35	6.86e−02	3.20	2.10e−02	3.16	3.50e−02	2.96	1.28e−01
75	3.39	4.66e−02	3.55	7.72e−02	3.44	5.12e−02	3.40	3.29e−02	3.25	5.90e−02
76	3.31	4.07e−02	3.46	4.67e−02	3.55	1.72e−02	3.56	2.63e−02	3.50	9.21e−02
77	3.38	2.25e−02	3.52	3.52e−02	3.52	3.07e−02	3.51	3.40e−02	3.35	7.26e−02
78	3.90	4.38e−02	3.94	4.00e−02	3.85	3.30e−02	3.77	4.30e−02	3.64	4.00e−02
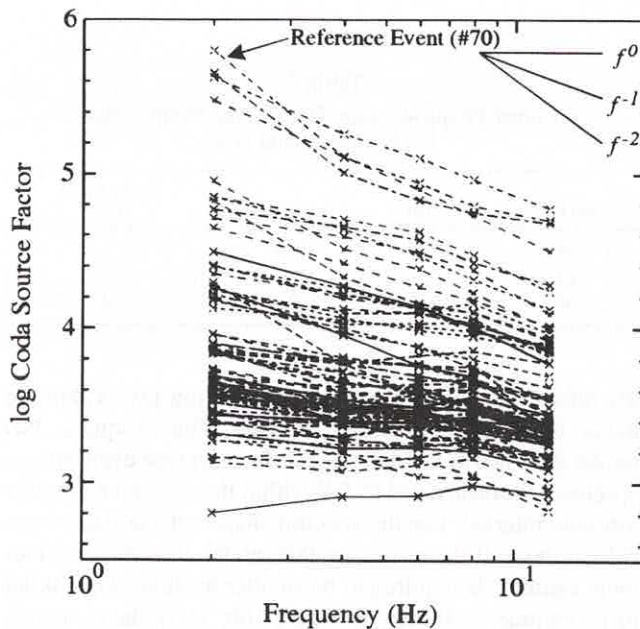
Figure 5.   Source spectra for each of the 78 events constructed from the five frequency-specific source factor estimates. Each spectral curve has been corrected to displacement.

spectral ratio curves for four scaling models (for specific δ, Υ, and $\omega_{0,r}$ values). Figure 8 shows four different families of spectral ratio curves as solid curves. For any given plot each successive curve denotes a decrease of the moment ratio by a factor of 10. Superimposed over each theoretical model are source spectral ratios taken with respect to event 70, with a corner frequency of 1.0 Hz. In all, three reference events, each with three different corner frequencies (mean and mean ± uncertainty), have been tested. Clearly, the ω-

cube, CSD model does not fit the data. Testing using two other reference events (events 58 and 62) also demonstrates a poor fit of both ω-cube, CSD and ω-cube, ISD models to the data. However, resolution of a best fit between the two ω-square models is not possible using the spectral ratio method alone.

To resolve the remaining model ambiguity we turn to the absolute scaling of the source estimates. Establishing the absolute scaling requires knowledge of the corner frequency and moment of at least one of the reference events from the data set. Unfortunately, none of the events had an independently determined moment. The largest event (event 70) was assigned M_S and m_b values of 4.1 and 4.4, respectively, by the National Earthquake Information Center (NEIC). To estimate the moment of this reference event, we determined an empirical relation between moment and magnitude for the region. Thirty regional earthquakes in Idaho, offshore Oregon and California, Vancouver Island, and the Queen Charlotte Islands (see Table 6 for event parameters) were selected using magnitudes assigned by the NEIC and moments from published Harvard CMT solutions. All event parameters were obtained from the U.S. Geological Survey *Preliminary Determination of Epicenter* (PDE) listings. A semi-log plot of M_0 versus M_S is shown in Figure 9 for these 30 events. Linear regression of $\log M_0$ on M_S gives the following magnitude-moment relation:

$$\log M_0 = (1.00 \pm 0.05) M_S + (19.21 \pm 0.25). \quad (12)$$

The regression correlation coefficient is 0.97. Extrapolating the linear trend of equation (12) to the assigned surface-wave magnitude for event 70, we estimate a moment of 2.0×10^{23} dyne-cm. This extrapolation appears valid since event
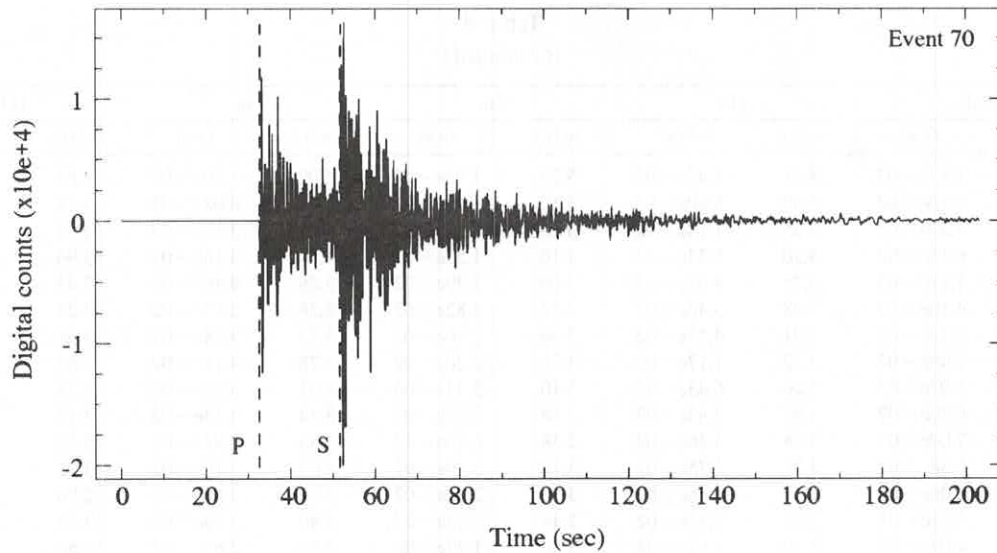
Figure 6.   Example seismogram recorded by the 5-sec (intermediate-period) instruments used for the corner frequency determinations of events 58, 62, and 70. The trace displayed is from event 70. The data window start time is arbitrarily set to zero, as absolute timing was not set in these records.
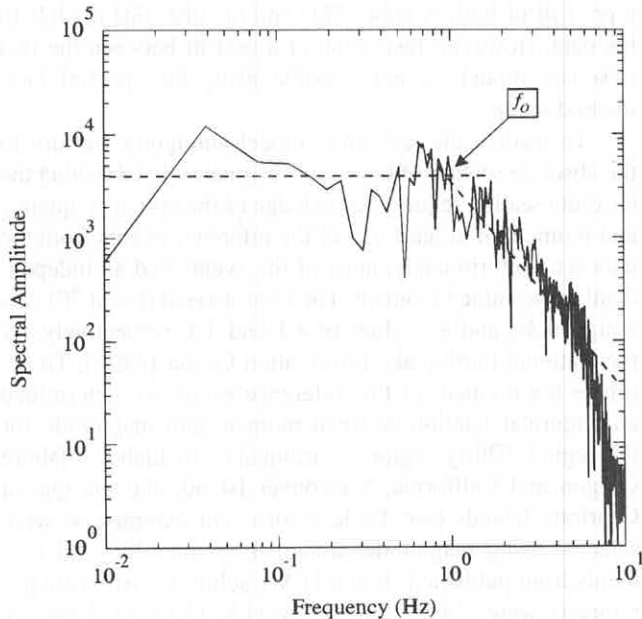
Figure 7.   A sample displacement spectrum from an intermediate-period record showing the corner frequency, f_0, as implied by the intersection of the flat low-frequency and high-frequency roll-off regions of the spectrum.

Table 5
Corner Frequencies for Three Large Events from Intermediate-Band Data

Event ID	f_0(Hz)	$\pm \delta f_0$(Hz)	No. of Stations Used
58	1.5	0.5	2
62	1.0	0.4	4
70	1.0	0.4	4

the reference event source spectrum falling just within the lower limit of the moment estimate. The ω-square, ISD model does not fit the data well if the reference event source spectrum is constrained to fall within the reference moment estimate interval. For the spectral shapes of the data to approach those of the ω-square, ISD model, the reference moment estimate is required to be smaller by at least one order of magnitude, as shown by Figure 10b. Thus, the ω-square, CSD model is best supported by the data.

Scalar Moment Estimates

With one event of known corner frequency and seismic moment and an appropriate scaling model, the source factor estimates can be directly related to seismic moment by solving equation (11) for the non–reference event moment, M_0 in terms of all of the known quantities:

$$M_0^3 - M_0^2 M_{0,r}(3C + B^3C^3) + 3M_0 M_{0,r}^2 C^2 - M_{0,r}^3 C^3 = 0, \quad (13)$$

where $B = (\omega/\omega_{0,r})^2$, $C = (R(\omega))/(1 + B)$, and $R(\omega)$ is the source factor spectral ratio of equation (11). Substituting val-

70 is quite near the lower end of the data used to establish the linear relation.

With this benchmark moment, we are able test the two remaining ω-square scaling models for agreement with our source factor estimates. As shown in Figure 10a, the ω-square, CSD model is a good empirical fit to the data with

(a)

(b)

Figure 4. (a) Quantile-quantile plot of the residuals for 8430 coda amplitude data from the least-squares inversion. The deviation from a straight line with a slope of 1 implies a non-Gaussian distribution. (b) Quantile-quantile plot of the residuals for the original 8430 amplitude data less 70 of the largest absolute residual values. The reduced data set residual distribution is nearly Gaussian. See text for details on quantile-quantile plotting.

estimates for the model parameters $\log I_j$ and $\log S_i(f)$. The assumption of constant data variance made using the classic least-squares approach, while convenient, is not necessarily justified. However, the jackknife method assumes no *a priori* knowledge or constraint of the data variance and simply maps the inherent variance in the data to the model param-

eters. Therefore, we prefer to use the error estimates produced using the jackknife method. Tables 3 and 4 show the model-parameter estimates, $\log I_j$ and $\log S_i(f)$, along with the associated jackknife error estimates. All values given are log-transformed quantities.

With the five source factor estimates for each event from the least-squares inversion, we construct a narrow region of the source spectrum after correcting the response to displacement; Figure 5 shows the resulting displacement source spectra for all events. The slopes of these spectra generally range from -2 for the largest events to zero for the smallest event, though some show considerable deviation. This trend reflects the typical corner frequency shift with moment inherent in the far-field scaling models.

Scaling Law Constraint

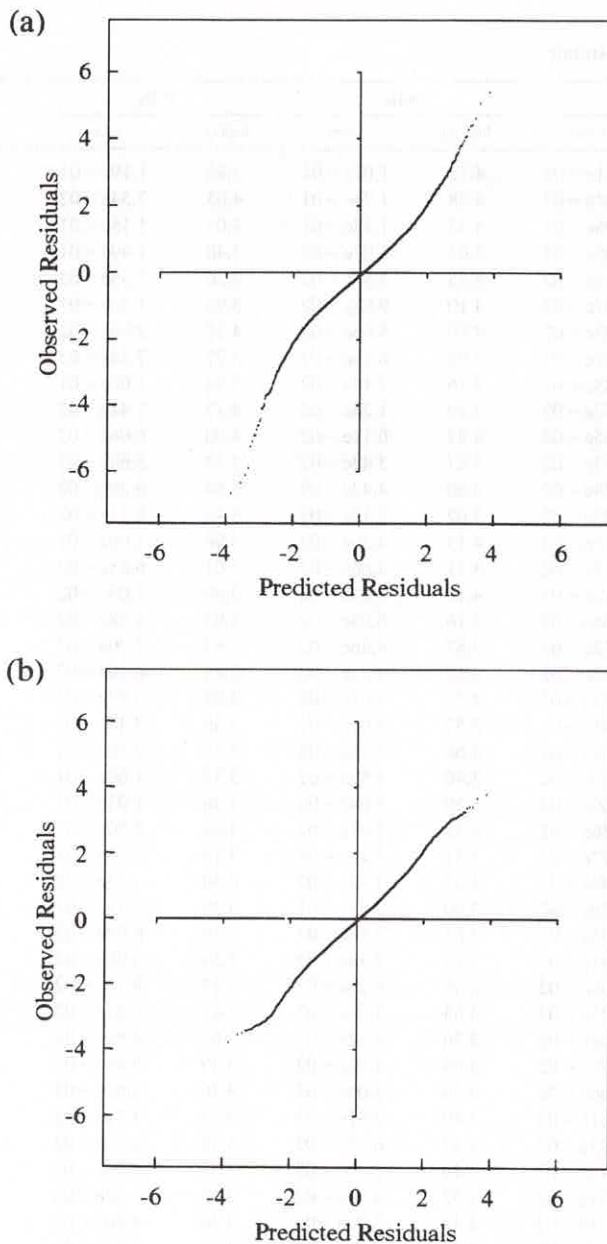To select an appropriate regional source scaling model, we apply a spectral ratio method as discussed by Chael (1987) to the source factor estimates returned from the inversion. Aki and Chouet (1975) showed that the ratio of the source spectra, Ω_1/Ω_2, for two different earthquakes is given by the ratio of the coda source factors, S_1/S_2. Given a reference event, we define $R^2(\omega)$ as the ratio of the squares of the coda source factors of the reference event, $S_r(\omega)$, and any other event, $S(\omega)$. $R^2(\omega)$ can be expressed in terms of the moments using equations (3) and (4):

$$R^2(\omega) \equiv \frac{|S(\omega)|^2}{|S_r(\omega)|^2} = \left[\frac{M_0}{M_{0,r}}\right]^2$$
$$\cdot \left[\frac{1 + \left(\frac{\omega}{\omega_{0,r}}\right)^2}{1 + \left[\frac{M_0}{M_{0,r}}\right]^{2/\delta} \cdot \left(\frac{\omega}{\omega_{0,r}}\right)^2}\right]^Y, \quad (11)$$

where $\omega_{0,r}$ is the reference event corner frequency, and Y and δ are model dependent constants to be determined. A *priori* knowledge of a reference event corner frequency is required to use the spectral ratio method, so estimates of corner frequencies for the three largest events were made using the direct-S and S-coda portions of each intermediate-period seismogram. Figure 6 shows an example raw seismogram for event 70. To estimate corner frequencies, we employed a standard spectral method. Each seismogram is windowed from the S arrival to the signal end. Windowed data are demeaned, tapered, and transformed to the frequency domain, and the corner frequency is estimated by inspection from the intercept of the flat low-frequency and high-frequency roll-off regions of the spectrum. Figure 7 shows a sample displacement spectrum with the inferred corner frequency. Estimates of the corner frequencies for events 58, 62, and 70 are determined using as many as four displacement spectra. Table 5 gives the resulting corner frequencies for these three events.

Using equation (11), we generate and plot families of

Table 4
Source Factor Estimates

ID	2 Hz $\log S_i(f)$	$(\pm\sigma)$	4 Hz $\log S_i(f)$	$(\pm\sigma)$	6 Hz $\log S_i(f)$	$(\pm\sigma)$	8 Hz $\log S_i(f)$	$(\pm\sigma)$	12 Hz $\log S_i(f)$	$(\pm\sigma)$
1	4.49	5.36e − 02	4.43	2.27e − 02	4.29	6.51e − 02	4.13	1.07e − 01	3.85	1.19e − 01
2	4.40	1.80e − 01	4.41	1.33e − 01	4.28	7.34e − 02	4.28	1.76e − 01	4.05	7.54e − 02
3	4.95	6.75e − 02	4.66	4.44e − 02	4.54	1.05e − 01	4.35	1.12e − 01	4.07	1.15e − 01
4	4.29	7.45e − 02	3.93	2.51e − 02	3.74	5.05e − 02	3.63	5.07e − 02	3.40	1.49e − 01
5	4.77	1.07e − 01	4.81	7.45e − 02	4.73	5.54e − 02	4.55	5.87e − 02	4.36	7.35e − 02
6	4.41	6.00e − 02	4.35	8.99e − 02	4.29	9.27e − 02	4.10	9.65e − 02	3.98	1.33e − 01
7	4.85	9.24e − 02	4.86	5.79e − 02	4.78	3.53e − 02	4.60	5.65e − 02	4.32	8.94e − 02
8	4.18	5.42e − 02	4.15	5.57e − 02	4.03	3.97e − 02	3.92	6.75e − 02	3.77	7.54e − 02
9	4.22	5.76e − 02	4.18	4.38e − 02	4.19	5.85e − 02	4.16	7.14e − 02	3.94	1.06e − 01
10	4.71	6.14e − 02	4.74	2.67e − 02	4.65	1.92e − 02	4.50	1.26e − 02	4.17	7.41e − 02
11	4.82	6.96e − 02	4.49	4.32e − 02	4.32	3.65e − 02	4.22	6.11e − 02	4.00	6.06e − 02
12	4.19	6.97e − 02	4.12	5.01e − 02	4.04	4.03e − 02	3.87	3.43e − 02	3.53	3.66e − 02
13	3.89	2.39e − 02	3.87	2.46e − 02	3.82	1.98e − 02	3.80	4.42e − 02	3.64	6.30e − 02
14	3.65	2.38e − 02	3.68	2.89e − 02	3.73	2.45e − 02	3.62	6.15e − 02	3.40	8.11e − 02
15	4.25	3.65e − 02	4.25	2.46e − 02	4.25	4.17e − 02	4.15	4.30e − 02	3.96	1.00e − 01
16	2.81	8.03e − 02	3.07	6.81e − 02	3.07	5.18e − 02	3.11	4.66e − 02	3.01	6.88e − 02
17	4.40	7.36e − 02	4.37	5.29e − 02	4.29	3.12e − 02	4.18	6.53e − 02	3.90	7.09e − 02
18	4.19	8.88e − 02	4.28	5.65e − 02	4.25	5.64e − 02	4.16	6.08e − 02	3.93	5.38e − 02
19	3.86	4.66e − 02	3.94	1.84e − 02	3.91	3.15e − 02	3.87	4.46e − 02	3.62	7.70e − 02
20	3.60	4.73e − 02	3.64	2.42e − 02	3.66	2.83e − 02	3.59	4.65e − 02	3.48	6.18e − 02
21	4.35	2.44e − 02	4.38	2.36e − 02	4.29	2.23e − 02	4.23	3.01e − 02	4.02	5.77e − 02
22	3.59	5.25e − 02	3.67	4.17e − 02	3.62	3.01e − 02	3.52	5.01e − 02	3.36	7.48e − 02
23	3.47	2.22e − 02	3.58	3.55e − 02	3.61	4.18e − 02	3.66	2.48e − 02	3.45	4.90e − 02
24	3.66	5.73e − 02	3.54	3.99e − 02	3.55	7.60e − 02	3.46	4.59e − 02	3.33	1.60e − 01
25	3.62	1.70e − 02	3.66	4.66e − 02	3.71	3.60e − 02	3.59	5.66e − 02	3.46	1.05e − 01
26	4.65	5.27e − 02	4.57	2.73e − 02	4.42	2.36e − 02	4.31	2.81e − 02	4.09	8.00e − 02
27	3.68	5.21e − 02	3.66	1.43e − 02	3.61	1.27e − 02	3.51	3.19e − 02	3.19	2.56e − 02
28	3.83	4.69e − 02	3.87	3.65e − 02	3.76	3.52e − 02	3.65	4.74e − 02	3.40	4.33e − 02
29	3.83	3.51e − 02	3.80	3.44e − 02	3.78	3.60e − 02	3.60	2.93e − 02	3.39	7.15e − 02
30	3.84	1.97e − 02	3.83	2.95e − 02	3.73	5.05e − 02	3.63	5.52e − 02	3.36	6.99e − 02
31	3.96	5.40e − 02	3.97	7.15e − 02	3.91	5.51e − 02	3.79	2.36e − 02	3.53	6.98e − 02
32	3.55	3.66e − 02	3.66	2.72e − 02	3.65	1.69e − 02	3.68	5.26e − 02	3.52	8.72e − 02
33	3.57	4.50e − 02	3.69	2.76e − 02	3.69	1.45e − 02	3.63	4.00e − 02	3.47	5.24e − 02
34	3.96	1.61e − 02	3.92	2.88e − 02	3.85	3.04e − 02	3.76	1.17e − 02	3.63	4.86e − 02
35	3.57	3.54e − 02	3.63	4.17e − 02	3.66	4.70e − 02	3.59	4.54e − 02	3.39	2.84e − 02
36	3.46	3.41e − 02	3.44	2.12e − 02	3.39	3.66e − 02	3.40	7.06e − 02	3.26	3.69e − 02
37	3.64	6.76e − 02	3.64	3.22e − 02	3.58	2.81e − 02	3.49	2.97e − 02	3.32	7.71e − 02
38	3.39	4.20e − 02	3.45	4.24e − 02	3.53	4.43e − 02	3.47	6.77e − 02	3.38	8.94e − 02
39	3.63	2.58e − 02	3.63	2.79e − 02	3.60	2.93e − 02	3.49	2.76e − 02	3.33	8.19e − 02
40	3.65	3.09e − 02	3.63	1.86e − 02	3.63	1.57e − 02	3.52	3.86e − 02	3.38	5.52e − 02
41	4.85	3.02e − 02	4.79	1.80e − 02	4.62	3.71e − 02	4.44	3.72e − 02	4.20	4.20e − 02
42	3.40	7.66e − 02	3.42	4.32e − 02	3.42	1.89e − 02	3.36	3.71e − 02	3.26	5.17e − 02
43	3.84	3.61e − 02	3.93	3.36e − 02	3.98	1.91e − 02	3.98	5.67e − 02	3.86	5.58e − 02
44	3.52	5.81e − 02	3.56	6.64e − 02	3.51	1.46e − 02	3.49	3.27e − 02	3.36	8.01e − 02
45	3.68	4.62e − 02	3.78	1.60e − 02	3.80	2.43e − 02	3.77	1.25e − 02	3.64	5.91e − 02
46	3.86	2.24e − 02	3.74	2.97e − 02	3.52	4.41e − 02	3.34	2.62e − 02	3.22	4.73e − 02
47	3.60	5.37e − 02	3.56	2.35e − 02	3.46	2.51e − 02	3.42	4.87e − 02	3.09	1.24e − 01
48	4.27	3.78e − 02	4.11	5.96e − 02	3.92	3.74e − 02	3.81	5.73e − 02	3.44	6.62e − 02
49	3.52	1.93e − 02	3.57	1.51e − 02	3.58	2.05e − 02	3.58	5.25e − 02	3.44	6.17e − 02
50	3.62	2.40e − 02	3.61	1.66e − 02	3.56	3.64e − 02	3.41	4.83e − 02	3.36	2.71e − 02
51	3.90	4.06e − 02	3.95	5.48e − 02	3.93	4.05e − 02	3.84	2.18e − 02	3.71	7.26e − 02
52	5.65	2.72e − 02	5.16	2.88e − 02	4.99	2.54e − 02	4.87	3.35e − 02	4.76	3.85e − 02
53	3.72	2.33e − 02	3.74	3.87e − 02	3.74	7.68e − 03	3.72	2.49e − 02	3.57	4.42e − 02
54	3.28	7.18e − 02	3.34	4.44e − 02	3.31	3.48e − 02	3.17	3.83e − 02	2.90	1.45e − 01
55	3.55	4.84e − 02	3.58	3.48e − 02	3.58	2.01e − 02	3.58	4.89e − 02	3.45	1.22e − 01
56	3.69	5.39e − 02	3.69	3.55e − 02	3.65	1.80e − 02	3.60	3.10e − 02	3.36	5.38e − 02
57	3.27	7.02e − 02	3.40	4.34e − 02	3.40	3.51e − 02	3.38	2.64e − 02	3.27	4.24e − 02
58	5.48	3.29e − 02	5.26	3.05e − 02	5.06	4.17e − 02	4.85	1.74e − 02	4.58	5.45e − 02
59	3.56	3.88e − 02	3.60	4.04e − 02	3.63	3.04e − 02	3.61	3.23e − 02	3.52	5.44e − 02
60	3.58	3.89e − 02	3.62	3.58e − 02	3.62	4.42e − 02	3.51	4.89e − 02	3.33	8.56e − 02
61	3.13	3.05e − 02	3.23	2.86e − 02	3.27	2.88e − 02	3.28	3.47e − 02	3.04	5.72e − 02

times exceeding 43 sec while using the Havskov *et al.* parameters for shorter lapse times.

Source Spectra and Site Responses

For source factor and site response estimates, we apply the single-scattering coda model of Aki and Chouet (1975) assuming body-wave scattering. An additional term is included, $I_j(f)$, which allows for variations in the site response. The coda amplitude as recorded by a given instrument is then given by

$$A_{ij}(f, t) = S_i(f)I_j(f)t^{-1}\exp\left(\frac{-\pi ft}{Q}\right), \qquad (5)$$

where i and j are source and site indices, respectively. Taking the base 10 logarithm (log) of both sides of equation (5) results in a linear system of equations, $\mathbf{Gm} = \mathbf{d}$, where $\mathbf{m}$ is a vector of unknown log-transformed source factors and site responses, and $\mathbf{G}$ is a sparse coefficient matrix. We impose two constraints on the system. First, the site responses are assumed to be frequency independent. This simplifies the problem by reducing the number of unknown model parameters. Though not necessary, this convenient simplification is used as an initial starting point in testing our source-parameter estimation procedure. The validity of this assumption is dependent on whether all stations involved are founded on rock sites. Table 3 includes a description of the local geology at each site. Most stations are on hard rock. Further discussion on the issue is deferred to the discussion section. The second constraint imposed provides absolute scaling for the site responses. Rather than assume a value for a particular site, the geometric mean of the site responses is set to zero,

$$\sum_j \log I_j = 0. \qquad (6)$$

As an example, for measurements from two events recorded at two stations using two frequency bands, the system takes the following matrix form:

$$
\begin{bmatrix}
1 & 0 & 1 & 0 & 0 & 0 \\
1 & 0 & 0 & 1 & 0 & 0 \\
0 & 1 & 1 & 0 & 0 & 0 \\
0 & 1 & 0 & 1 & 0 & 0 \\
1 & 0 & 0 & 0 & 1 & 0 \\
1 & 0 & 0 & 0 & 0 & 1 \\
0 & 1 & 0 & 0 & 1 & 0 \\
0 & 1 & 0 & 0 & 0 & 1 \\
1 & 1 & 0 & 0 & 0 & 0
\end{bmatrix}
\begin{bmatrix}
\log I_1 \\
\log I_2 \\
\log S_1(f_1) \\
\log S_1(f_2) \\
\log S_2(f_1) \\
\log S_2(f_2)
\end{bmatrix}
=
\begin{bmatrix}
\hat{A}_{11}(f_1, t) \\
\hat{A}_{11}(f_2, t) \\
\hat{A}_{12}(f_1, t) \\
\hat{A}_{12}(f_2, t) \\
\hat{A}_{21}(f_1, t) \\
\hat{A}_{21}(f_2, t) \\
\hat{A}_{22}(f_1, t) \\
\hat{A}_{22}(f_2, t) \\
0
\end{bmatrix},
\qquad (7)
$$

where $\hat{A}_{ij}$ is the log of the coda amplitude measurement corrected for both geometrical spreading and attenuation. A least-squares inversion is used to solve simultaneously for $\log S_i(f)$ and $\log I_j$, giving optimal estimates for these quan-

tities, under the assumption of independent errors with zero mean and equal variance.

For non-Gaussian error distributions, variance of the least-squares estimates may be artificially large. Least-squares estimates are adversely affected by a small number of outliers (e.g., Egbert and Booker, 1986). To check the validity of a Gaussian error assumption and to identify outliers, we plot the distribution of the actual residuals observed for the full inversion against those expected for a Gaussian distribution in a normal probability or quantile-quantile (Q-Q) plot (Goodall, 1983). The quantiles of the residuals are just the ordered residuals themselves. The quantiles of the Gaussian distribution are given by $\Phi^{-1}(i/n)$, where Φ^{-1} is the inverse of the Gaussian function, i is the sample index, and n is the total number of samples in the ordered residuals. As an example, with $n = 100$, the fifth residual, $r(5)$, would correspond to $\Phi^{-1}(0.05) = -2.00$, so that the point plots in the Q-Q plot as $[-2.00, r(5)]$. If the observed residual distribution is truly Gaussian, the Q-Q plot should approximate a straight line with a unit slope. Figure 4a shows the resulting Q-Q plot for the full problem (using all 8430 measurements). The deviation from a straight line indicates the residual distribution is non-Gaussian, with the largest residuals larger than expected. After removing 70 data values ($<1.0\%$ of the total) corresponding to the largest absolute residuals, the inversion was rerun, and the resulting Q-Q plot produced is shown in Figure 4b. In this case, the reduced data set residual distribution appears to fit a Gaussian distribution. In the final analysis, the model estimates are generated from the reduced data set of 8360 measurements.

Estimates of the model errors for the above inversion are considered using two different techniques. First, we consider the classic least-squares approach. Here, the data are assumed to be uncorrelated with a constant variance of σ^2. The model variances are the diagonal elements of the covariance matrix, where $cov[\mathbf{m}] = \sigma^2 (\mathbf{G}^T\mathbf{G})^{-1}$ (Menke, 1984). A drawback to this approach is the required generation of the matrix $(\mathbf{G}^T\mathbf{G})^{-1}$, which can be difficult because of the large amounts of storage space required for a large matrix $\mathbf{G}$. We also consider the jackknife estimates of model variance for error estimation (Efron and Tibshirani, 1993). For jackknife estimates the data are grouped into l subsets, and the inversion is performed l separate times using $n - n/l$ of the original data, excluding a different subset each time. The model parameters derived from each of the l inversions are denoted $\hat{m}_j$. From these l inversion model parameters, pseudovalues $\tilde{m}_j$ are created from the weighted sum

$$\tilde{m}_j = l\hat{m}_{\text{all}} - (l - 1)\hat{m}_j, \qquad (8)$$

where $\hat{m}_{\text{all}}$ are the model parameters from the full inversion. The jackknifed estimate $\tilde{m}$ of the model parameter is the mean of the following pseudovalues:

Table 3
Station Locations and Associated Site Responses

Station Name	Lat. (°N)	Long. (°W)	Elevation (km)	Site Rock Type	Site Response (log l_i)	Std. Error ($\pm\sigma$)
APW	46.6517	122.6475	0.457	andesite	−0.242	1.27e−02
ASR	46.1507	121.5927	1.280	andesite	0.122	2.00e−02
BHW	47.8368	122.0322	0.198	basalt, gabbro	−0.416	2.64e−02
BLN	48.0074	122.9718	0.585	basalt, breccia	0.143	7.39e−03
BOW	46.4750	123.2281	0.870	basalt	0.092	1.78e−02
CDF	46.1162	122.0475	0.780	volcanoclastic	0.115	1.46e−02
CMM	46.4353	122.5058	0.620	andesite	0.135	1.42e−02
CMW	48.4237	122.1190	1.190	sedimentary	0.247	1.07e−02
CPW	46.9738	123.1363	0.792	basalt	0.0646	1.05e−02
EDM	46.6388	122.1500	1.609	andesite	0.367	8.53e−03
ELK	46.3056	122.3408	1.270	dacite	−0.0902	1.12e−02
FL2	46.1964	122.3503	1.378	andesite	−0.182	9.04e−03
FMW	46.9416	121.6698	1.859	dacite	0.338	4.54e−03
GHW	47.0417	122.2725	0.268	glacial till	−0.379	1.28e−02
GLK	46.5639	121.6085	0.268	volcanic sediments	−0.241	1.32e−02
GMW	47.5479	122.7863	0.0506	basalt	0.0412	1.08e−02
HDW	47.6485	123.0542	1.006	basalt, breccia	0.278	1.29e−02
HTW	47.8035	121.7691	0.829	andesite, breccia	0.276	9.53e−03
JCW	48.1952	121.9253	0.792	sedimentary	0.423	2.98e−03
KOS	46.4613	122.1905	0.828	volcanoclastic	0.104	1.46e−02
LMW	46.6680	122.2913	1.195	andesite	0.00737	1.24e−02
LO2	46.7500	121.8100	0.853	volcanoclastic	−0.241	1.13e−02
MBW	48.7840	121.8997	1.676	sedimentary	0.153	1.19e−02
MCW	48.6797	122.8323	0.693	sedimentary	0.0577	6.83e−03
MEW	47.2019	122.6458	0.098	glacial till	−0.625	1.87e−02
NEL	48.0783	120.3382	1.490	granodiorite	−0.0291	2.49e−02
OBH	47.2362	123.8658	0.938	basalt, breccia	−0.161	1.88e−02
OHW	48.3233	122.5318	0.054	glacial till	−0.514	5.74e−03
ONR	46.8771	123.7712	0.257	basalt, sedimentary	−0.264	3.47e−02
OSD	47.8208	123.7017	2.010	sedimentary	−0.369	1.03e−02
PGW	47.8219	122.5994	0.122	glacial till	−0.232	1.76e−02
RCS	46.8710	121.7311	2.877	volcanoclastic	−0.318	4.58e−02
RER	46.8192	121.8409	1.756	andesite	−0.118	3.61e−02
RMW	47.4597	121.8053	1.024	andesite, breccia	0.400	7.23e−03
RPW	48.4483	121.5136	0.850	greenschist	0.452	1.17e−02
RVC	46.9429	121.9715	1.000	sedimentary	0.450	1.64e−02
RVW	46.1495	122.7437	0.460	andesite	−0.283	3.04e−02
SHW	46.1974	122.2357	1.399	volcanic sediment	−0.0201	3.14e−02
SMW	47.3195	123.3417	0.840	basalt, breccia	−0.0550	1.46e−02
SOS	46.2440	122.1367	1.270	volcanoclastic	0.201	4.94e−02
SPW	47.5537	122.2459	0.008	sedimentary	−0.558	2.13e−02
STD	46.2378	122.2227	1.268	volcanic sediments	−0.0710	3.86e−02
STW	48.1508	123.6703	0.308	basalt	−0.0984	2.01e−02
TBM	47.1695	120.5983	1.064	basalt	−0.0402	1.32e−02
TDL	46.3508	122.2158	1.400	dacite	0.0436	7.18e−03
WAT	47.6986	119.9542	0.900	eolian sediments	0.731	1.76e−02
WPW	46.6982	121.5467	1.250	volcanoclastic	0.306	8.80e−03

$$\bar{m} = \frac{1}{l} \sum_{j=1}^{l} \tilde{m}_j, \qquad (9)$$

and has variance given by

$$\sigma_{\text{jack}}^2 = \frac{\sum \tilde{m}_j^2 - \frac{1}{l}\left(\sum \tilde{m}_j\right)^2}{l(l-1)}. \qquad (10)$$

From the variance, the standard error is σ_{jack}. While choosing $l = n$ would appear to give the best jackknife estimates, a large number for l requires a large number of "mini" inversions. As a matter of practicality, our choice for l is 12. Q-Q plots of the 12 separate "mini" inversion residuals show distributions similar to that shown in Figure 4b supporting a Gaussian error distribution assumption and validating the use of the classic least-squares approach in solving the "mini" inversions.

Using each of the above methods, we generate error

Table 1

(*Continued*)

Event ID	Date (m/d/yr)	Origin Time (GMT)	Lat. (°N)	Long. (°W)	Depth (km)	Mag. (M_c)	Mag. (M)	M_0 (dyne-cm)
62[†]	12/24/1989	08:45:58.90	46.65	122.12	18.45	4.9	5.1	4.4e + 23
63	01/02/1990	14:54:06.88	47.10	122.08	10.10	2.7	2.8	1.8e + 20
64	01/15/1990	14:00:57.14	47.42	122.09	19.39	2.6	2.8	2.0e + 20
65[†]	02/15/1990	18:34:59.15	47.92	121.92	16.34	3.4	3.4	1.4e + 21
66	02/20/1990	23:11:01.76	47.00	123.04	44.51	3.0	3.0	3.2e + 20
67	03/06/1990	01:55:66.46	47.47	122.03	14.94	2.6	2.7	1.1e + 20
68	03/17/1990	08:39:36.82	47.32	122.30	6.77	3.0	3.0	3.9e + 20
69	03/26/1990	01:27:18.34	46.85	121.91	10.74	3.0	3.0	3.6e + 20
70[†]	04/14/1990	05:33:26.16	48.88	122.18	2.67	5.0	4.8	2.0e + 23
71	07/27/1990	22:00:34.54	47.64	122.48	22.28	3.0	2.8	2.0e + 20
72	11/21/1990	10:51:18.93	47.98	122.78	15.96	2.6	2.7	1.2e + 20
73[†]	12/30/1990	02:20:56.99	47.47	121.81	17.07	3.5	3.4	1.4e + 21
74	03/04/1991	20:07:18.73	47.59	122.75	17.17	2.5	2.6	8.8e + 19
75	03/16/1991	20:16:59.28	47.24	122.67	49.47	2.6	2.8	1.6e + 20
76	03/17/1991	19:34:42.28	47.62	121.94	22.35	2.7	2.8	1.9e + 20
77	03/22/1991	23:01:29.33	47.40	122.08	6.00	2.6	2.8	1.8e + 20
78	05/16/1991	02:39:49.35	46.76	121.90	11.34	3.0	3.1	5.2e + 20

[†] Events used to determine applicability of the Havskov et al. (1989) coda Q model.
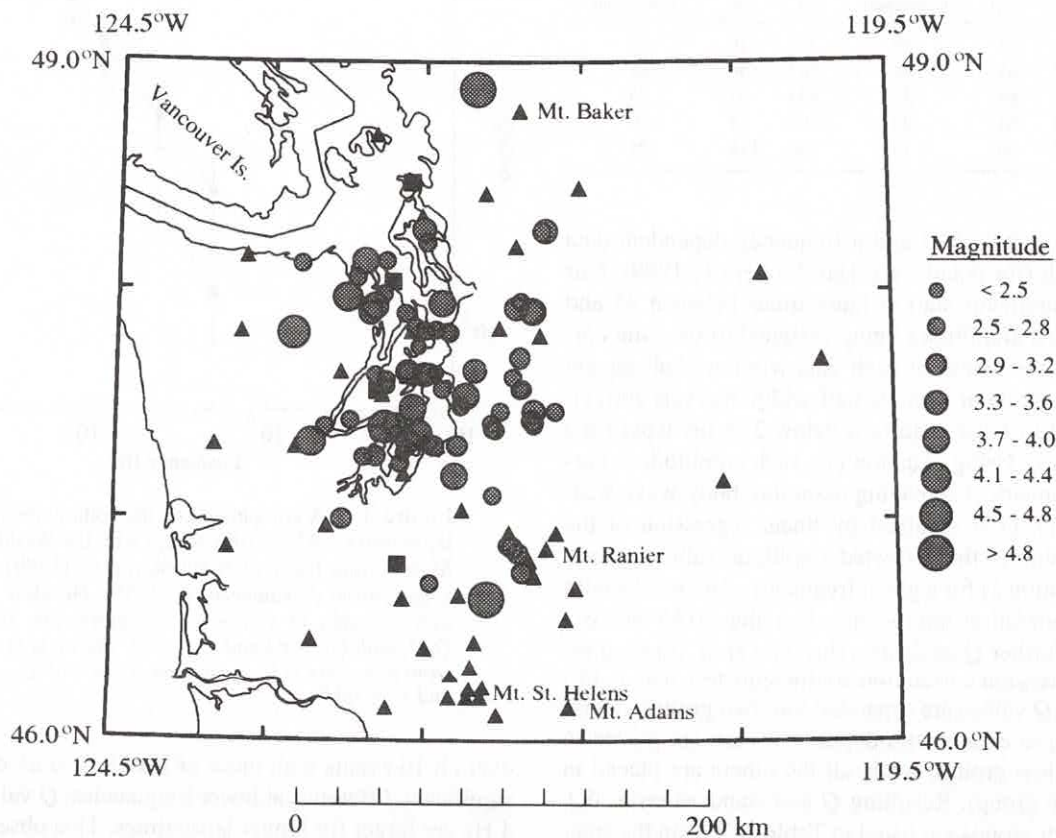

Figure 1.   Locations of earthquakes and PNSN stations used in this study. Earthquake epicenters are denoted by circles, short-period stations by triangles, and intermediate-period temporary stations by squares.
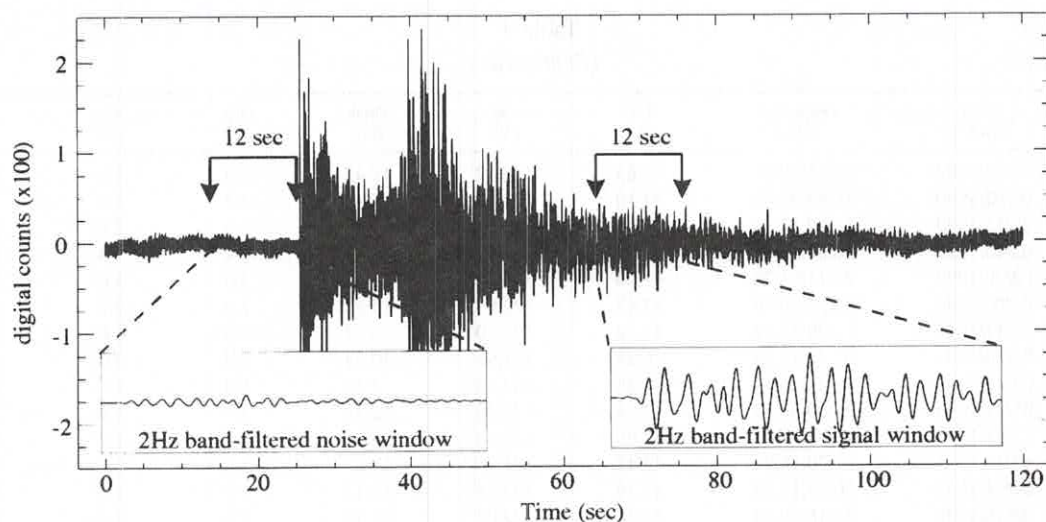
Figure 2. A sample short-period seismogram showing the tapered, band-filtered 12-sec windows from which presignal noise and signal measurements are made. Rms amplitudes are calculated from the center 5 sec of each window.

Table 2

Coda Q Study Results for Lapse Times >43 sec

Frequency (Hz)	Z < 30 km			Z ≥ 30 km		
	Q	$\pm\delta Q$	No. of Measurements	Q	$\pm\delta Q$	No. of Measurements
2.0	227	53	27	226	39	37
4.0	343	64	34	362	58	35
6.0	427	84	34	454	65	33
8.0	524	84	25	560	78	29
12.0	717	96	14	760	118	24

different filter bandwidths and a frequency-dependent data window length (for details, see Havskov *et al.*, 1989). Our Q coda measurements start at lapse times between 45 and 60 sec with rms amplitudes being assigned to the time corresponding to the center of each data window. Subsequent measurements occur at window half-width intervals until either the signal-to-noise ratio falls below 3 or the lapse time exceeds 120 sec. Using equation (1), each amplitude is corrected for geometrical spreading assuming body-wave scattering ($v = 1$). Q is obtained by linear regression of the natural logarithm of the corrected amplitude value on lapse time (see equation 2) for a given frequency. Any results with regression correlation coefficients less than 0.65 are excluded from further Q analysis. (Havskov *et al.* rejected results with regression correlation coefficients less than 0.45.) The resulting Q values are separated into two groups. Those corresponding to events with depths <30 km are placed in group 1 (shallow group), while all the others are placed in group 2 (deep group). Resulting Q and standard error, δQ, values for both groups are listed in Table 2. Within the standard errors in Q for deep and shallow events, we find no difference in the Q values and thus no depth dependence in Q. As shown in Figure 3, a comparison of the mean Q values
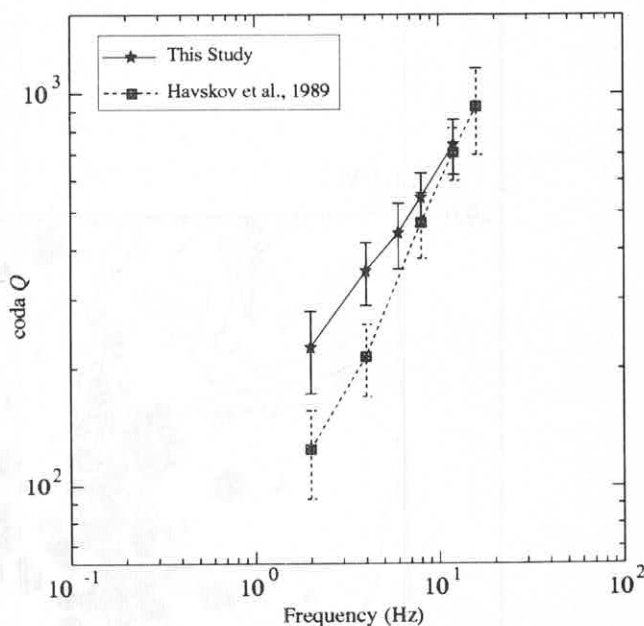
Figure 3. A comparison of the coda Q results for lapse times >43 sec (this study) with the Washington State average reported by Havskov *et al.* (1989) shows a lapse-time dependence in Q. The Havskov *et al.* average coda Q values fit the power-law relation $Q_0 f^a$, with $Q_0 = 63$ and $a = 0.97$. The coda Q values from this study fit the same power law with $Q_0 = 142$ and $a = 0.66$.

over all 16 events with those of Havskov *et al.* does show a significant difference at lower frequencies; Q values at 2 and 4 Hz are larger for longer lapse times. This observed difference may be due to multiple scattering. We conclude that Q is lapse-time dependent and therefore apply our parameters (in Table 2) to coda amplitude measurements with lapse

frequency, k is a proportionality constant, and Υ is related to the rate of decrease (roll-off) of the spectrum at high frequencies (Aki and Richards, 1980). Most kinematic source models proposed have either ω^{-2} (Aki, 1967; Brune, 1970) or ω^{-3} high-frequency roll-off (Aki, 1967; Savage, 1972). These two models are denoted in equation (3) by $\Upsilon = 2$ and $\Upsilon = 3$, respectively, and are commonly referred to as ω-square and ω-cube models. The differences between these two models are rooted in the nature of their source time functions.

A second important feature of a far-field scaling model is the functional dependence between seismic moment and corner frequency. Aki (1967) proposed that $M_0 \propto \omega_0^{-3}$. For $L \propto \omega_0^{-1}$, where L is the fault dimension, and an average fault displacement that scales linearly with L (and is constant with moment), this model implies a constant stress drop with increased moment (self-similarity) and a stress drop that is inversely proportional to the cube of L. Nuttli (1983) suggested that self-similarity is valid for interplate earthquakes, but he argued from observations that a second model with a stress drop that increases with moment, $M_0 \propto \omega_0^{-4}$, applies to intraplate earthquakes. These two models relating seismic moment and corner frequency can be expressed by

$$M_0 \cdot \omega_0^\delta = \text{constant}, \qquad (4)$$

where $\delta = 3$ for a constant stress drop (CSD) model, and $\delta = 4$ for an increased stress drop (ISD) model (Chael, 1987). In order to estimate seismic moment using coda amplitude as a measure of the source spectrum, we must establish a suitable regional scaling model. This requires estimating Υ and δ from equations (3) and (4) and knowledge of the site effects for all stations included in this study.

Data

For the coda amplitude analysis we use a data set consisting of 78 western Washington earthquakes recorded by up to 47 1-Hz vertical-component stations within the PNSN. Digital data are acquired at a nominal rate of 100 samples/sec. Events were selected to provide a uniform hypocentral distribution, including both crustal ($z < 30$ km, 61 events) and subcrustal ($30 \leq z < 65$ km, 17 events) earthquakes. Duration magnitudes, M_c, for the events included in the data set range from 2.4 to 5.0; Table 1 gives earthquake location parameters for the 78 events used here, and Figure 1 shows earthquake epicenters and all stations included in this study. The station locations are given in Table 3. A comprehensive review of the PNSN data acquisition, general operation, and station distribution is given by Ludwin *et al.* (1994).

From each short-period seismogram, two 12-sec windows are extracted, one for coda amplitude determination and the other for estimation of background noise. The data window is typically centered at twice the S lapse time, a time considered well into the established coda decay envelope (Rautian and Khalturin, 1978). In cases where signals are

clipped at twice the S lapse time because of the limited dynamic range of the short-period instruments, longer lapse times are used. The noise window is centered at 6 sec before the P arrival. Figure 2 shows a typical short-period record of a local earthquake with each window noted. We apply a 10% cosine taper to the ends of each window, then each window is narrow-bandpass-filtered in the time domain at each of five center frequencies (2.0, 4.0, 6.0, 8.0, and 12.0 Hz) using a five pole Chebyshev type II filter. We chose constant bandwidth filters with a width of 2.0 Hz. Since all of the filters pass the same energy, amplitude corrections between the different filters are unnecessary.

A root-mean-square (rms) amplitude is generated using the central 5 sec of each window. For the data window, the lapse time corresponding to the window center marks the time of the rms amplitude measurement. Rms amplitudes from both windows are used to determine a signal-to-noise ratio as a means of estimating data quality.

To address the issue of noise, we tested the following synthetic signals: a "noise-free" signal assumed to be a cosine function, a noise signal assumed to be Gaussian white noise, and a "noisy" signal comprising the sum of the two. For these three signals we established the contribution of noise to the total signal rms amplitude for a given ratio of rms signal to rms noise, and we found that for an rms signal-to-noise ratio of 3.33, the difference between the "noise-free" data and "noisy" data rms amplitudes is less than 4.0%. On that basis, we accepted only those coda amplitude measurements with an rms signal-to-noise ratio exceeding 3. A total of 8430 amplitude measurements, with lapse times ranging from 10 to 120 sec, met this criterion and qualified for analysis.

Three of the largest earthquakes in the data set, events 58, 62, and 70 from Table 1, were also recorded by up to four temporary intermediate-band, three-component stations (Kinemetrics SH-1 and SV-1 sensors). Each intermediate-band station has a high-dynamic-range Sprengnether DR-200 digital recorder for the three channels of data recording at a rate of 20 samples/sec. Locations of these stations are also shown in Figure 1. The intermediate-band data are used for corner frequency determination, a parameter essential for far-field scaling model constraint.

Analysis

Coda Q Modeling

A subset of 16 larger events (noted in Table 1 by a superscript dagger) recorded at five PNSN stations (CPW, HDW, HTW, LMW, and SMW) is used to determine the applicability of the Havskov *et al.* (1989) coda Q model for lapse times exceeding 43 sec. To ensure the comparability of our results with those of Havskov *et al.*, we follow their procedure for amplitude measurement only for the coda Q model determination. Their method of amplitude measurement deviates from the one outlined above, with slightly

Table 1
Local Earthquakes used for Coda Amplitude Analysis

Event ID	Date (m/d/yr)	Origin Time (GMT)	Lat. (°N)	Long. (°W)	Depth (km)	Mag. (M_c)	Mag. (M)	M_o (dyne-cm)
1	04/16/1980	14:47:06.79	48.13	122.90	50.10	3.8	3.5	2.3e+21
2	04/27/1980	06:00:27.61	47.37	122.56	20.18	3.7	3.6	2.8e+21
3	06/08/1980	22:40:10.65	47.97	123.02	48.54	4.2	3.9	6.7e+21
4	06/23/1980	16:05:16.43	47.54	122.05	0.05	3.7	3.1	5.9e+20
5	09/19/1980	22:53:16.28	47.91	121.82	4.40	3.8	4.1	1.5e+22
6	09/21/1980	17:45:12.97	47.91	121.82	3.15	3.5	3.5	2.0e+21
7[†]	11/12/1981	18:10:25.35	47.94	122.40	26.58	3.7	4.1	1.8e+22
8	11/26/1981	12:30:01.08	47.65	122.62	21.95	3.5	3.3	9.6e+20
9	04/14/1982	07:22:43.63	47.63	122.52	27.28	3.4	3.4	1.6e+21
10[†]	08/28/1983	12:47:47.97	47.93	122.84	51.50	3.9	4.0	9.6e+21
11[†]	10/31/1983	21:47:58.81	47.34	123.24	43.36	4.3	3.7	3.6e+21
12	06/02/1984	12:57:20.99	47.41	122.70	21.49	3.6	3.3	8.5e+20
13	12/17/1984	08:30:12.57	47.27	122.83	46.30	3.2	3.1	4.9e+20
14	01/01/1985	19:15:00.80	46.88	121.96	11.31	3.1	2.9	2.9e+20
15	01/11/1985	13:07:57.13	47.90	122.87	21.32	3.3	3.5	1.8e+21
16	01/29/1985	20:39:27.23	47.43	121.80	17.55	2.7	2.5	5.1e+19
17[†]	02/28/1985	17:02:04.40	47.49	122.59	47.08	3.7	3.5	2.2e+21
18	03/18/1985	17:15:55.26	47.34	122.62	53.30	3.5	3.5	1.7e+21
19	06/16/1985	10:22:59.25	47.43	121.83	17.03	3.1	3.1	5.7e+20
20	03/11/1986	07:23:21.05	47.34	122.49	7.24	2.9	2.9	2.6e+20
21[†]	03/28/1986	04:12:46.70	48.26	121.73	2.32	3.6	3.6	2.4e+21
22	05/04/1986	20:14:00.50	47.82	122.51	24.82	2.6	2.9	2.4e+20
23	06/17/1986	20:30:44.53	47.47	121.67	16.65	2.6	2.9	2.4e+20
24	06/29/1986	23:40:25.35	47.79	123.16	15.42	2.7	2.8	2.1e+20
25	06/30/1986	01:03:27.18	47.84	122.58	19.74	2.7	2.9	2.7e+20
26[†]	07/08/1986	05:16:32.48	48.26	122.52	61.82	3.5	3.7	4.3e+21
27	08/31/1986	18:31:59.11	47.37	122.81	27.03	2.9	2.9	2.4e+20
28	11/07/1986	10:35:54.67	48.12	123.32	42.16	2.6	3.0	3.8e+20
29	12/09/1986	10:06:20.13	47.65	122.63	18.42	2.6	3.0	3.6e+20
30	01/15/1987	17:58:13.18	47.83	122.44	19.55	2.7	3.0	3.6e+20
31	03/17/1987	16:34:54.58	48.26	121.76	3.28	2.8	3.1	5.6e+20
32	04/07/1987	15:25:01.88	47.50	122.28	25.69	2.6	2.9	2.8e+20
33	04/15/1987	31:22:10.64	47.49	122.28	22.87	2.5	2.9	2.8e+20
34	04/28/1987	06:42:46.51	47.61	122.76	20.37	2.8	3.1	5.2e+20
35	06/26/1987	14:42:38.01	47.81	122.35	14.95	2.7	2.9	2.5e+20
36	07/25/1987	10:10:18.48	47.43	122.99	15.60	2.7	2.8	1.5e+20
37	08/06/1987	21:12:42.55	48.13	122.76	22.44	2.7	2.9	2.3e+20
38	09/14/1987	04:24:12.27	46.72	122.47	18.40	2.6	2.8	1.7e+20
39	09/20/1987	08:53:13.20	48.06	122.95	55.42	2.8	2.9	2.3e+20
40	01/26/1988	03:13:38.01	47.41	121.82	19.69	2.9	2.9	2.4e+20
41[†]	03/11/1988	10:01:26.04	47.19	122.32	64.72	3.9	4.0	9.6e+21
42	05/27/1988	06:12:58.66	47.29	122.66	20.99	2.5	2.7	1.4e+20
43[†]	06/16/1988	11:05:04.79	47.71	121.89	7.51	3.1	3.2	7.6e+20
44	09/08/1988	13:47:13.35	48.20	122.50	23.12	2.8	2.8	2.0e+20
45[†]	10/23/1988	00:04:19.97	47.82	122.36	19.23	2.8	3.0	4.0e+20
46	10/29/1988	08:47:04.81	47.63	122.83	47.12	2.9	2.9	2.7e+20
47	11/29/1988	04:13:56.82	47.57	122.40	10.44	2.6	2.8	1.8e+20
48	01/17/1989	13:55:28.82	47.65	122.19	1.53	3.3	3.2	7.9e+20
49	01/19/1989	12:21:42.24	47.57	121.90	2.68	2.7	2.9	2.2e+20
50	01/19/1989	12:34:12.91	47.57	121.88	2.27	2.7	2.9	2.1e+20
51	02/21/1989	06:48:21.66	47.32	122.46	15.97	3.0	3.1	5.9e+20
52[†]	03/05/1989	06:42:00.66	47.81	123.36	46.17	4.5	4.7	1.3e+23
53[†]	04/11/1989	16:32:59.98	47.27	122.91	47.06	2.8	3.0	3.6e+20
54	04/17/1989	09:52:03.02	47.76	122.55	21.72	2.5	2.6	9.8e+19
55	04/21/1989	09:40:43.70	47.39	122.06	4.50	2.8	2.9	2.3e+20
56	05/25/1989	01:27:28.92	47.37	122.69	19.86	2.8	2.9	2.7e+20
57	05/31/1989	12:46:57.43	47.95	121.89	17.83	2.6	2.7	1.3e+20
58[†]	06/18/1989	20:38:37.89	47.41	122.78	44.75	4.4	4.7	1.2e+23
59	06/19/1989	22:05:55.80	46.89	121.98	8.55	2.7	2.9	2.5e+20
60	09/04/1989	06:34:54.44	47.90	122.64	17.51	2.7	2.9	2.2e+20
61	10/29/1989	12:08:36.69	47.64	122.44	25.18	2.4	2.6	8.9e+19